

REVISITING THE GREAT ATTRACTOR: THE LOCAL GROUP'S STREAMLINE TRAJECTORY, COSMIC VELOCITY AND DYNAMICAL FATE

RICHARD STISKALEK 

Astrophysics, University of Oxford, Denys Wilkinson Building, Keble Road, Oxford, OX1 3RH, UK

HARRY DESMOND 

Institute of Cosmology & Gravitation, University of Portsmouth, Dennis Sciama Building, Portsmouth, PO1 3FX, UK

STUART MCALPINE 

The Oskar Klein Centre, Department of Physics, Stockholm University, Albanova University Center, 106 91 Stockholm, Sweden

GUILHEM LAVAUX 

CNRS & Sorbonne Université, Institut d'Astrophysique de Paris (IAP), UMR 7095, 98 bis bd Arago, F-75014 Paris, France

JENS JASCHE 

The Oskar Klein Centre, Department of Physics, Stockholm University, Albanova University Center, 106 91 Stockholm, Sweden

MICHAEL J. HUDSON 

Department of Physics and Astronomy, University of Waterloo, Waterloo, ON N2L 3G1, Canada
Waterloo Centre for Astrophysics, University of Waterloo, Waterloo, ON N2L 3G1, Canada
Perimeter Institute for Theoretical Physics, Waterloo, ON N2L 2Y5, Canada

Version February 17, 2026

Abstract

We revisit the Great Attractor using the **Manticore-Local** suite of digital twins of the nearby Universe. The Great Attractor concept has been proposed as an answer to three distinct questions: what sources the Local Group velocity in the cosmic microwave background frame, where present-day velocity streamlines converge, and where the Local Group is moving to. Addressing the original motivation of the Great Attractor—explaining the Local Group cosmic velocity—we find that mass within $155 h^{-1}$ Mpc accounts for only $\sim 72\%$ of that velocity magnitude with ~ 38 deg directional offset. We show that even in the purely linear regime convergence within this volume is not guaranteed, particularly when also accounting for small-scale contributions to the observer velocity; no single structure, including the proposed Great Attractor, would be expected to dominate the velocity budget. Streamline convergence is smoothing-scale-dependent, transitioning from Virgo at small scales through the Hydra-Centaurus region at intermediate scales to Shapley at large scales; at intermediate smoothing the convergence point lies near Abell 3565 with an asymmetric basin of mass $\log(M/(h^{-1} M_{\odot})) = 16.4 \pm 0.1$ that excludes Norma. To address the third question, we evolve the **Manticore-Local** realisations to scale factor $a = 10$ in a new **Beyond-Present-Time** simulation suite and identify the asymptotic future location of the Local Group. We find that the dominant motion is towards Virgo, but even it contributes at most one third of the Local Group velocity. Our results demonstrate that the classical Great Attractor is not a dynamically dominant structure but an artefact of the instantaneous velocity field, and that no single attractor is likely to account for the Local Group motion in the cosmic rest frame.

Subject headings: Cosmography, dynamics of the Local Group, peculiar velocities, Great Attractor

1. INTRODUCTION

A key component of observational astrophysics is cosmography, the mapping out of nearby structures in the Universe. While this is most readily done using the luminosities at various wavelengths of galaxies and clusters,

complementary information is provided by galaxies' *velocities*, which encode their trajectories and hence provide information about their past and future. This is necessary to build a detailed picture of the dynamics of the local Universe and the components thereof.

An important role in this endeavour is played by *attractors*, massive objects or collections of objects which domi-

nate the gravitational field in large volumes of space. As hierarchical structure formation proceeds, such objects become richer over time while surrounding regions—the voids—become emptier. The most obvious attractors are the superclusters readily visible to optical telescopes, including Virgo, Coma and Shapley. However, other attractors are more difficult to identify, for example because they are located in the Zone of Avoidance (ZoA) behind the disk of the Milky Way, where dust obscuration makes optical astronomy difficult. Velocity information provides an effective means of identifying such structures, as infall toward them can be detected in unobscured neighbouring regions (Lilje *et al.* 1986; Lynden-Bell *et al.* 1988; Pomarède *et al.* 2017; Kraan-Korteweg *et al.* 2017; Courtois *et al.* 2019; Pomarède *et al.* 2020).

An obscured structure of particular interest is the *Great Attractor* (GA), the focus of this paper. The GA emerged in the late 1980s as a large-scale density enhancement inferred from peculiar-velocity surveys of galaxies, motivated by the need to explain the peculiar velocity of the Local Group (LG) with respect to the cosmic microwave background (CMB) (Smoot *et al.* 1977). Dressler *et al.* (1987) measured peculiar velocities of elliptical galaxies and fitted a bulk flow, noting that the Hydra–Centaurus region itself appeared to be moving toward mass concentrations beyond $\sim 5000 \text{ km s}^{-1}$. Earlier work by Aaronson *et al.* (1982) had already identified deviations from pure Hubble expansion, though without locating a definitive source for the observed motion. Similarly, Lilje *et al.* (1986) detected a significant quadrupolar tidal velocity field in the Local Supercluster caused by external density structure, with the dominant eigenvector pointing toward Hydra–Centaurus. Building on this, Lynden-Bell *et al.* (1988) fitted an attractor model and identified the GA as a large-scale overdensity at $(\ell, b) \approx (307, 9)$ deg at a distance of $43.5 h^{-1} \text{ Mpc}$, located beyond Hydra–Centaurus in order to explain its motion. We shall later refer to this as the “classical” Great Attractor.

Subsequent analyses refined this picture. Hudson (1993a) mapped the density field from optical galaxies, showing that the overdensity in the Centaurus–Hydra–Pavo–Virgo supercluster complex peaks near the Centaurus cluster (Cen 30) at a distance of $35 h^{-1} \text{ Mpc}$, not at the GA distance of $43.5 h^{-1} \text{ Mpc}$. Hudson (1993b) used this density field to predict the LG peculiar velocity, finding a ~ 30 deg misalignment with the CMB dipole direction. Hudson (1994a) concluded that there is no evidence for a GA within $80 h^{-1} \text{ Mpc}$ being primarily responsible for the motion of nearby galaxies, with $\gtrsim 400 \text{ km s}^{-1}$ attributable to sources beyond this distance. This density-field approach, mapping the galaxy distribution and predicting peculiar velocities via linear theory, was further developed by Pike and Hudson (2005) and Carrick *et al.* (2015), and extended to full Bayesian inference of the initial conditions by Jasche and Lavaux (2019), providing the foundation for the digital twins used in this work. However, a large portion of the GA region lies behind the ZoA, making direct optical observation of galaxies difficult due to dust obscuration and stellar confusion and hence necessitating velocity-based analysis. In this context, the GA came to be understood not as the sole driver of the CMB dipole, but as an important inter-

mediate overdensity embedded within a larger-scale flow pattern extending to greater depths.

Despite these challenges, subsequent measurements reinforced the notion of a coherent inflow to the GA region. Using Fundamental Plane and Tully–Fisher distance indicators, Dressler and Faber (1990a,b) and Burstein *et al.* (1990) found evidence for a convergence of peculiar velocities near $4000\text{--}4500 \text{ km s}^{-1}$, consistent with the inferred distance to the GA. However, Hudson (1994b) showed that inhomogeneous Malmquist bias can mimic such convergence; after correcting for this effect, the data are better described by infall of $\sim 240 \text{ km s}^{-1}$ onto Cen 30 combined with a residual bulk dipole of $\sim 360 \text{ km s}^{-1}$, with no need for convergence at the GA distance. Nevertheless, the amplitude and extent of the measured bulk flows posed a significant challenge to cold dark matter (CDM) models at the time. *N*-body simulations by Bertschinger and Juskiewicz (1988) showed that the mass concentration required to produce such motions was improbable in CDM scenarios assuming standard galaxy biasing, suggesting that the GA could impose non-trivial constraints on large-scale structure formation models.

The current understanding is that the GA is not a gravitationally bound object but a diffuse overdense region influencing galaxy motions on $\sim 100 h^{-1} \text{ Mpc}$ scales. Within this region, the Norma cluster (Abell 3627) has been thought to be a plausible core. Identified through HI and near-infrared observations obscured by the Milky Way, Norma was found to be a rich and massive cluster located at $(\ell, b) \approx (325, -7)$ deg and $cz \approx 4870 \text{ km s}^{-1}$ (Kraan-Korteweg *et al.* 1996). Subsequent dynamical analysis by Woudt *et al.* (2008) confirmed its significance, though the GA’s mass distribution does not converge neatly on Norma, suggesting a broader structure. Another massive cluster hidden behind the ZoA is the Vela supercluster, though it is considerably further away than the GA with a recessional velocity of $18,000 \text{ km s}^{-1}$ (Kraan-Korteweg *et al.* 2017; Courtois *et al.* 2019; Hatamkhani *et al.* 2023; Rajohnson *et al.* 2024). The South Pole Wall, at $cz \approx 12,000 \text{ km s}^{-1}$, is another large-scale structure detected through peculiar-velocity analysis (Pomarède *et al.* 2020).

Several studies pointed to the necessity of considering other large-scale overdensities in understanding the peculiar motion of the LG. The Perseus–Pisces supercluster was identified as another prominent structure contributing comparably to the density field within the same volume. In some interpretations, Perseus–Pisces itself appears to be moving in the direction of the GA, implying the influence of more massive structures beyond, such as the Shapley Supercluster (Scaramella *et al.* 1989; Raychaudhury 1989). These findings challenged the notion of the GA as a unique attractor and instead indicated that it may form part of a broader hierarchy of flows, a picture that our results will further substantiate.

Modern reconstructions of the large-scale velocity field, particularly with the CosmicFlows programme, have offered a more nuanced picture (Courtois *et al.* 2013; Tully *et al.* 2014, 2019; Courtois *et al.* 2023; Tully *et al.* 2023; Hoffman *et al.* 2024; Courtois *et al.* 2025). They have shifted the definition of the GA: whereas the original formulation by Lynden-Bell *et al.* (1988) sought a massive overdensity whose gravitational influence would explain

the LG’s peculiar velocity, more recent work defines the GA through streamline convergence and the associated *watershed basin* within which velocities flow toward a common attractor. [Courtois et al. \(2013\)](#) first presented velocity-field streamlines in the GA region, and [Tully et al. \(2014\)](#) subsequently used such streamlines to define watershed basins. [Valade et al. \(2024\)](#) used Hamiltonian Monte Carlo techniques on CosmicFlows-4 data to identify basins of attraction out to $30,000 \text{ km s}^{-1}$, finding a slight preference for placing the GA within the basin of the more massive Shapley attractor. Their analysis identifies the dominant basin with the Sloan Great Wall, occupying a volume of $15.5 \times 10^6 (h^{-1} \text{ Mpc})^3$. [Dupuy et al. \(2025\)](#) develop a deep-learning-based method for reconstructing the local density and peculiar velocity fields, calculating a 64% probability of the existence of the GA as a unique watershed structure. These results align with the view that the GA basin lies along a filamentary path feeding into more distant mass concentrations, and may not be a particularly significant region in its own right.

The classification of superclusters has evolved accordingly. The Laniakea supercluster, which encompasses the GA convergence point, was originally proposed by [Tully et al. \(2014\)](#) and is treated as one of several watershed basins in the local Universe by [Dupuy and Courtois \(2023\)](#). While initially characterised as a coherent basin, its membership and boundaries remain ambiguous; recent reconstructions indicate that it may in fact lie on the periphery of the more massive Shapley basin ([Valade et al. 2024](#)). These revised interpretations cast the GA not as a final destination of local flows but as a transition point along a larger trajectory. As such, the classical image of a single dominant attractor gives way to a network of interacting flows and gravitational basins. This also reflects the ongoing challenge of explaining the LG’s velocity of 620 km s^{-1} relative to the CMB ([Planck Collaboration et al. 2020a](#))—the original motivation for the GA concept—which cannot be fully accounted for by attraction toward known overdensities alone. In this context, [Hoffman et al. \(2017\)](#) introduced the complementary concept of “repellers”, in particular proposing the “Dipole Repeller” as a large underdensity roughly opposite to Shapley also contributing to the LG’s velocity. The GA concept thus carries an inherent ambiguity among three distinct physical questions: what mass distribution sources the LG’s peculiar velocity in the CMB frame (the original motivation of [Lynden-Bell et al. 1988](#)), where the present-day velocity field converges (the streamline approach), and in what direction the LG will actually move in the future.

These three definitions need not coincide. Galaxies do not continue along their present-day streamlines indefinitely because these lines depict instantaneous velocities while the evolving mass distribution of the Universe causes velocities to change over time, so that actual dynamics may diverge significantly from the streamline picture. Indeed, in a dark-energy-dominated universe with low Ω_m , perturbation growth freezes out and structures decouple from the Hubble flow only if already bound, making the present velocity field encapsulated in streamlines a particularly misleading indicator of future trajectories. An alternative approach is numerical action orbit modelling ([Shaya et al. 1995, 2017, 2022](#)), which computes past and future trajectories of galaxies within a

Λ -cold dark matter (Λ CDM) universe.

In this paper, we explicitly construct the GA according to all three definitions using a new reconstruction of the local Universe based on the *Bayesian Origin Reconstruction from Galaxies* algorithm (BORG; [Jasche and Wandelt 2013; Jasche and Lavaux 2019](#)), in particular the *Manticore-Local* implementation ([McAlpine et al. 2025](#)), which infers the initial and final density fields of the local $\sim 200 h^{-1} \text{ Mpc}$ by applying a sophisticated Bayesian forward model to the number density of galaxies in the 2M++ catalogue ([Lavaux and Hudson 2011](#)). The velocity field derived therefrom has been shown to surpass other reconstructions by a substantial margin in accuracy ([Stiskalek et al. 2025; McAlpine et al. 2025](#)) and is therefore expected to afford a corresponding gain in GA characterisation accuracy. We apply the streamline method to these data, inferring the properties of the GA and also investigating its smoothing-scale dependence, which we find to be considerable (e.g. [Dupuy et al. 2019, 2020](#)). We also propose a new *dynamical* definition of the GA which, instead of assessing streamline convergence at fixed present time, explores the full trajectories of objects over cosmic history and into the future. Zooming in further, the high-resolution BORG-based reconstructions of the LG neighbourhood by [Wempe et al. \(2024, 2025\)](#) are particularly well suited to studying the future evolution of the Milky Way.

The structure of the paper is as follows. In Section 2 we describe the BORG reconstructions that form the basis of our study and the catalogue of clusters that we investigate in a GA context. In Section 3 we present our methodology, both for streamline convergence (Section 3.1) and our new dynamical definition involving simulations evolved beyond the present time (Section 3.2). In Section 4 we distinguish three definitions of the GA, and present the results of our streamline and future dynamics analyses. Section 5 concludes. All logarithms are base-10.

2. DATA

In Section 2.1, we describe the *Manticore-Local* digital twin suite, which provides a probabilistic reconstruction of the local Universe. In Section 2.2, we describe a set of random Λ CDM simulations used to quantify the reconstruction volume necessary to capture the LG motion. In Section 2.3, we present a compiled galaxy cluster catalogue used to identify observed structures in the GA region.

2.1. Digital twins of the local Universe

We employ the *Manticore-Local* suite of digital twins,¹ which provides a high-fidelity reconstruction of the local Universe out to approximately 200 Mpc from the Milky Way ([McAlpine et al. 2025](#)). *Manticore-Local* is based on the BORG algorithm ([Jasche and Wandelt 2013; Jasche and Lavaux 2019](#)) applied to the 2M++ galaxy catalogue ([Lavaux and Hudson 2011](#)) and constitutes the latest BORG-based re-

¹ Such digital twins are traditionally referred to as constrained simulations, however in our context a more precise name would be “data-constrained posterior simulations”, highlighting that the initial conditions are derived from a full Bayesian forward model and include explicit uncertainty quantification.

construction of the 2M++ volume. BORG produces a posterior distribution of initial density fields at $z = 1000$ on a 256^3 grid centred on the Milky Way in a $681 h^{-1}$ Mpc box by forward-modelling structure formation with a gravity solver, incorporating redshift-space distortions, selection effects, and galaxy biasing, and comparing the resulting redshift-space galaxy distribution to observations via a generalised Poisson likelihood (Jasche *et al.* 2015; Lavaux and Jasche 2016; Leclercq *et al.* 2017; Lavaux *et al.* 2019; Porqueres *et al.* 2019; Stopyra *et al.* 2024). Independent BORG posterior samples are post-processed by augmenting the inferred 256^3 initial conditions with random small-scale modes and then evolved to $z = 0$ with an N -body simulation, yielding the probabilistic ensemble of digital-twin realisations consistent with observed large-scale structure.

The **Manticore-Local** suite comprises 80 posterior samples resimulated with SWIFT (Schaller *et al.* 2024). The simulations adopt a $681 h^{-1}$ Mpc box centred on the Milky Way with uniform resolution on a 1024^3 mesh, yielding an initial condition spatial resolution of $0.67 h^{-1}$ Mpc and a particle mass of $2.4 \times 10^{10} h^{-1} M_{\odot}$. The cosmological parameters are drawn from the Dark Energy Survey Year 3 analysis (Abbott *et al.* 2022): $h=0.681$, $\Omega_m=0.306$, $\Omega_b=0.0486$, $\sigma_8=0.807$, and $n_s=0.967$, assuming the Λ CDM model. McAlpine *et al.* (2025); McAlpine (2025) demonstrated that **Manticore-Local** exhibits excellent agreement with observed cluster masses and positions, accurately reproduces the local velocity field, and matches Λ CDM predictions for the power spectrum and halo mass function.

The **Manticore-Local** suite provides density and velocity fields generated from the $z = 0$ particle distributions via smoothed particle hydrodynamics (Monaghan 1992; Colombi *et al.* 2007), with a minimum of 32 neighbours for the smoothing kernel. These fields are sampled on a 256^3 grid with voxel size $2.7 h^{-1}$ Mpc, sufficient for capturing the large-scale dynamics. In addition to analysing these present-day fields, we also evolve the **Manticore-Local** initial conditions beyond $z = 0$ to study the future dynamics of the local Universe by introducing the **Beyond-Present-Time** (BPT) simulation suite (see Section 3.2).

2.2. Random simulations

To quantify the reconstruction volume necessary to capture all contributions to the LG motion in the CMB frame, we employ a set of random Λ CDM simulations as a control sample. We use the fiducial set of **Quijote** simulations (Villaescusa-Navarro *et al.* 2020), comprising 15,000 N -body realisations in a $(1000 h^{-1} \text{Mpc})^3$ box with 512^3 particles. These were run with **Gadget-III** (Springel 2005) adopting a flat Λ CDM cosmology consistent with the *Planck* 2018 results (Planck Collaboration *et al.* 2020b): $h = 0.6711$, $\Omega_m = 0.3175$, $\Omega_b = 0.049$, $\sigma_8 = 0.834$, and $n_s = 0.9624$. The cosmological parameters differ slightly from those adopted in **Manticore-Local**, but we assume this difference is negligible for our comparative purposes.

We use the publicly available density fields at $z = 0$ sampled on a 256^3 grid with voxel size $3.9 h^{-1}$ Mpc, constructed using a piecewise cubic spline (PCS) mass assignment scheme. From these density fields, we compute

the corresponding linear theory velocity field in Fourier space as (Peebles 1980)

$$\mathbf{v}(\mathbf{k}) = -ifH(a)a\frac{\delta(\mathbf{k})\mathbf{k}}{k^2}, \quad (1)$$

where $f = \Omega_m^{0.55}$ is the dimensionless growth rate (Bouchet *et al.* 1995; Wang and Steinhardt 1998), $H(a)$ is the Hubble parameter, a is the scale factor, $\delta(\mathbf{k})$ is the Fourier transform of the overdensity field, and \mathbf{k} is the wave vector. For each simulation, we compute the observer velocity at the box centre sourced by all matter, \mathbf{V}_{box} , and by matter within radius R , $\mathbf{V}_{\text{inner}}(R)$. To compute $\mathbf{V}_{\text{inner}}(R)$, we mask the overdensity field to zero beyond R before transforming to Fourier space. Because the Fourier formulation implicitly assumes periodic boundary conditions, we pad the density field with empty cells by 50% of the box size on each side before computing the velocity field, thereby suppressing spurious contributions from periodic replicas. We compute both \mathbf{V}_{box} and $\mathbf{V}_{\text{inner}}(R)$ for all 15,000 simulations, sampling R from 10 to $300 h^{-1}$ Mpc in $10 h^{-1}$ Mpc increments.

2.3. Galaxy cluster catalogue

To characterise the GA and assess observed cluster membership, we adopt the cluster catalogue compiled by McAlpine *et al.* (2025) and supplement it with additional clusters in the GA region queried from the NASA/IPAC Extragalactic Database². The resulting catalogue includes well-studied clusters such as Centaurus, Hydra, and Norma in the GA region, along with surrounding structures including Virgo, Shapley, Perseus, and Coma. Of particular interest is the Centaurus-Crux cluster filament, comprising Centaurus, Abell 3565, Abell S0753, and Abell 3574, which we discuss in detail in Section 4.2. Table 1 lists the cluster positions in Galactic coordinates and their recession velocities.

3. METHODOLOGY

We adopt two complementary approaches to identify the GA-like structures. In Section 3.1, we integrate streamlines of the present-day velocity field to identify convergence points and partition the velocity field into basins of attraction, following standard methods from the literature (e.g. Dupuy *et al.* 2019, 2020, 2025). In Section 3.2, we evolve the **Manticore-Local** initial conditions forward in time to determine the long-term gravitational fate of structures in the local Universe.

3.1. Present-day velocity streamlines

Streamlines follow the scheme of Dupuy *et al.* (2019, 2020, 2025): test particles are initialised at voxel centres and advanced with a second-order Runge-Kutta (RK2) integrator using an adaptive temporal step that enforces a fixed spatial advance. We note that Dupuy *et al.* (2025) employ a higher-order Runge-Kutta integrator; we find this makes no substantial difference as we adopt small step sizes. Velocities at particle positions are obtained via trilinear interpolation of the smoothed grid. The RK2 update computes the velocity at the initial position, advances to an intermediate location, and evaluates

² <https://ned.ipac.caltech.edu>

TABLE 1
SELECTION OF GALAXY CLUSTERS CONSIDERED IN THIS WORK,
WITH A PREFERENCE FOR CLUSTERS IN THE GA REGION.
POSITIONS ARE GIVEN IN GALACTIC COORDINATES AND VELOCITIES
ARE CMB FRAME RECESSION VELOCITIES. COORDINATES ARE
ADOPTED FROM [McALPINE *et al.* \(2025\)](#) OR QUERIED FROM THE
NED DATABASE. MULTIPLE ENTRIES FOR HERCULES AND SHAPLEY
DENOTE DISTINCT CLUSTERS TRADITIONALLY CONSIDERED
MEMBERS OF THE RESPECTIVE SUPERCLUSTERS.

Name	ℓ [deg]	b [deg]	cz_{CMB} [km s $^{-1}$]
Ursa Major	144.57	65.5	1101
Fornax	236.7	-53.0	1332
Virgo	283.8	74.4	1636
Centaurus	302.4	21.6	3403
Hydra	269.6	26.5	4058
Abell 3565	313.5	28.0	4120
Abell S0753	320.3	28.4	4200
Pavo II	332.0	-24.0	4200
Abell 3574	317.5	30.9	4942
Norma	325.3	-7.1	4955
Perseus (A426)	150.6	-13.3	4995
Leo	235.1	73.0	6890
Abell 3581	323.1	32.9	7032
Coma	58.1	88.0	7463
Hercules (A2199)	62.9	43.7	9113
Abell 496	209.6	-36.5	9849
Hercules (A2063)	12.8	49.7	10634
Hercules (A2151)	31.6	44.5	11024
Hercules (A2147)	29.0	44.5	11072
Shapley (A3571)	316.3	28.6	11965
Abell 548	230.3	-24.8	12363
Abell 119	125.7	-64.1	13004
Abell 1736	312.6	35.0	13823
Abell 1644	304.9	45.4	14448
Shapley (A3558)	312.0	30.7	14784
Shapley (A3562)	313.3	30.4	15065

the velocity at that half-step position (denoted $\mathbf{v}[\mathbf{x}]$ for velocity evaluated at position \mathbf{x}):

$$\begin{aligned}\mathbf{x}(t_{i+1/2}) &= \mathbf{x}(t_i) + \frac{1}{2}\mathbf{v}[\mathbf{x}(t_i)]\Delta t_i, \\ \mathbf{x}(t_{i+1}) &= \mathbf{x}(t_{i+1/2}) + \mathbf{v}[\mathbf{x}(t_{i+1/2})]\Delta t_{i+1/2}.\end{aligned}\quad (2)$$

The temporal step maintains spatial increment Δs , such that

$$\Delta t = \frac{\Delta s}{|\mathbf{v}| + \epsilon},\quad (3)$$

with $\Delta s = 0.05\Delta x$ for voxel size Δx and $\epsilon = 10^{-6}$ km s $^{-1}$ to regularise vanishing velocities and avoid division by zero, yielding ~ 20 integration steps per voxel. We apply periodic boundary conditions, though all trajectories of interest remain in the central region of the box. The streamline integration is similar to the dynamical definition of attractors (presented next), except that the velocity field is fixed to the present-time snapshot rather than evolved self-consistently under gravity, and the trajectories correspond to test particles advected through this field. We assess convergence by monitoring particle displacement over a fixed fraction of the integration: the total number of steps is 25,000, and the monitoring

window spans 10% of them. A streamline is converged when its displacement within the window falls below half a grid cell; with the choice of 25,000 steps we find that all particles meet this criterion.

Converged positions are binned to voxels and grouped into basins by merging all neighbouring (face-sharing) voxels. Each component centroid is defined as the mean position of its member test particles, and the membership count measures the basin volume feeding that attractor. The observer (i.e. Milky Way or LG) convergence point is isolated by integrating a single streamline launched from the observer position, adopting the same convergence criterion. We smooth the velocity field with a Gaussian kernel of standard deviation σ_{smooth} , starting with no smoothing and then increasing the smoothing scale from 1 to 16 h^{-1} Mpc in steps of 1 h^{-1} Mpc, to isolate the large-scale flow while progressively suppressing small-scale fluctuations as σ_{smooth} is raised, and then follow streamlines over that smoothed field. Across smoothing scales, we shall find that this trajectory terminates in Virgo, the Classical *Great Attractor* (cGA), or Shapley, revealing how progressively stronger smoothing shifts the Milky Way streamline toward the larger-scale attractor. We distinguish the *GA convergence point* — the actual convergence location of streamlines — from the *GA basin*, which is the set of all locations whose streamlines terminate at the GA point. Note that this distinction is sometimes confused in the literature; for example the Laniakea supercluster, which [Tully *et al.* \(2014\)](#); [Dupuy and Courtois \(2023\)](#) treat as the basin associated with the GA, is simply the GA basin in our definition.

3.2. Simulating future dynamics of the Local Universe

The streamline approach described in Section 3.1 identifies attractors directly from the present-time velocity field and exploits the long-range correlation of the velocity field to extrapolate the velocity field into the ZoA. While operationally useful for partitioning the flow into basins, this snapshot-based method has fundamental limitations: streamline convergence points depend on the chosen smoothing scale, do not necessarily coincide with physical structures (i.e. gravitationally bound systems), and do not describe the actual trajectories of test particles under gravitational evolution. The instantaneous velocity field reflects the matter distribution at a single time slice and therefore cannot account for future mergers, the influence of dark energy, or the time-dependent strength of gravitational interactions.

A key advantage of *Manticore-Local* is that it reconstructs not only the present-day density and velocity fields but also the underlying initial conditions and the full dynamical evolution in between. This enables us to move beyond snapshot-based inferences and follow the genuine structure formation dynamics. By evolving the *Manticore-Local* initial conditions forward to a scale factor of $a = 10$, we allow gravitational interactions to unfold self-consistently and can identify which structures truly dominate the future evolution of the local Universe. We evolve 50 *Manticore-Local* realisations using the *Gadget4* ([Springel *et al.* 2021](#)) code with the same cosmology as *Manticore-Local*.³

³ The main *Manticore-Local* suite contains 80 posterior sam-

We choose $a = 10$ because structure formation effectively ceases as dark energy dominates the energy density (within the flat Λ CDM cosmology assumed by `Manticore-Local`; e.g. dynamical dark energy models would modify this timescale). We verify that the halo mass function no longer evolves significantly beyond $a = 2$. Since we only require the large-scale dynamics, we adopt a low-resolution simulation with 256^3 particles in a $681 h^{-1}$ Mpc box, corresponding to a particle mass of approximately $1.6 \times 10^{12} h^{-1} M_{\odot}$, sufficient to identify the cluster population in the local Universe.

We store particle snapshots at scale factors of 1, 2, 5, 10 (corresponding to ages of 13.8, 24.8, 40.4, 52.4 Gyr) and identify dark matter haloes at each snapshot using the `Gadget4` built-in friends-of-friends (FoF) halo finder (Davis *et al.* 1985) with a linking length of 0.2 times the mean inter-particle separation. We shall refer to this suite as the `Manticore-Local, Beyond-Present-Time` (BPT) suite.

4. RESULTS

We now present results from both approaches to identifying the GA. In Section 4.1, we analyse streamlines of the present-day velocity field to locate the GA and characterise its basin of attraction. In Section 4.2, we track the gravitational evolution of structures in the local Universe to determine their long-term fate. In Section 4.3, we assess which scales contribute to the LG velocity in the CMB frame.

As discussed above, the GA label mixes several related issues; to disentangle them, we distinguish three definitions:

1. *Classical Great Attractor (cGA)*: The large-scale velocity field structure identified historically from peculiar-velocity samples. Dressler *et al.* (1987) fitted a bulk flow (constant peculiar velocity), whereas Lynden-Bell *et al.* (1988) fitted an attractor model in which peculiar velocity falls off as a power law of distance from the attractor centre. More recent reconstructions (e.g. Dupuy *et al.* 2025) locate the cGA through streamline convergence of the present-day velocity field. Lynden-Bell *et al.* (1988) placed this near $(\ell, b) \approx (307, 9)$ deg at $\sim 43 h^{-1}$ Mpc, with Norma later proposed as the GA core at $(\ell, b) = (325.3, -7.1)$ deg and $50 h^{-1}$ Mpc (Kraan-Korteweg *et al.* 1996).
2. *Streamline Great Attractor (sGA)*: Either the true (model-dependent) observer streamline convergence point or its associated basin. The analyses referred to above identify the sGA convergence point with the cGA, although we find the sGA to be significantly smoothing-dependent: at intermediate smoothing ($\sigma_{\text{smooth}} \approx 3 h^{-1}$ Mpc) the sGA convergence point coincides with the cGA, but it transitions to Virgo at low smoothing and to Shapley at high smoothing. The cGA inferred by our analysis is therefore the sGA at such intermediate smoothing.

ples; we use 50 (randomly chosen) in the BPT for convenience. We verify that our results are not sensitive to this choice and that 50 posterior samples are sufficient.

3. *Dynamical Great Attractor (dGA)*: The asymptotic future displacement direction of the Milky Way under full gravitational evolution. We determine this by evolving constrained initial conditions of the local Universe beyond present-time in the BPT suite rather than integrating the frozen present-time velocity field as in the above definition. By evolving to $a = 10$, we identify which structures are gravitationally dominant and nearly bound to the LG; dark energy prevents full gravitational collapse, so we cannot follow trajectories to $a \rightarrow \infty$, but the dominant gravitational influences are already apparent by this epoch.

Note that while the sGA and dGA each have a basin associated with the convergence point, the cGA is typically defined as the convergence point itself. We do not consider the basin associated with the dGA (the region within which test particles all end up at the same place), so dGA will refer specifically to the convergence point henceforth.

4.1. Streamline analysis

We first examine the Milky Way streamline and its smoothing scale-dependence to localise the sGA within the `Manticore-Local` realisations. Following Dupuy *et al.* (2019, 2020), we identify the sGA convergence point by tracing a streamline from the observer (Milky Way or LG) position to its terminus. The streamlines shown in Fig. 1 display three convergence regimes: Virgo when $\lesssim 2 h^{-1}$ Mpc smoothing is applied, the cGA for $2 h^{-1}$ Mpc $\lesssim \sigma_{\text{smooth}} \lesssim 4 h^{-1}$ Mpc, and Shapley at high smoothing values. This occurs not because the location of the “drain”, i.e. the convergence point, is sensitive to the smoothing, but rather because the “mountain ranges” that separate watersheds are sensitive to smoothing: when the smoothing is sufficiently large, separate basins are merged together. For $\sigma_{\text{smooth}} = 2 h^{-1}$ Mpc, 30 of 80 Milky Way streamlines still terminate in Virgo, whereas all streamlines at either $\sigma_{\text{smooth}} = 3$ or $4 h^{-1}$ Mpc end at the cGA. At $\sigma_{\text{smooth}} = 8 h^{-1}$ Mpc, approximately 20% of the streamlines do not reach Shapley but instead typically terminate at $\sim 50 h^{-1}$ Mpc near $b \approx 0$ deg, i.e. in the ZoA. Given the incomplete knowledge of the large-scale structure, probabilistic treatments such as BORG are required to determine the plausible range of realisations compatible with the observed data.

Following streamlines from the observer position at smoothing scales of 2, 3 and $4 h^{-1}$ Mpc, we identify the cGA convergence point in each `Manticore-Local` realisation. Table 2 presents the inferred positions in Galactic coordinates (r, ℓ, b) . At $\sigma_{\text{smooth}} = 3 h^{-1}$ Mpc, the inferred cGA convergence point lies at distance $41_{-5}^{+2} h^{-1}$ Mpc and $(\ell, b) = (313_{-5}^{+1}, 27_{-4}^{+2})$ deg, close to Abell 3565 (see Table 1). Abell 3565 is part of a filamentary structure extending through Centaurus, Abell S0753 and Abell 3574, which are members of the Hydra–Centaurus Supercluster. This nexus of flows has been identified previously: the cluster grouping including Abell 3565, S0753, and Abell 3574 was discussed as part of the “four clusters” region by Courtois *et al.* (2013), and it marks the terminus of flows in the Laniakea basin defined by Tully *et al.* (2014); see also the flow lines com-

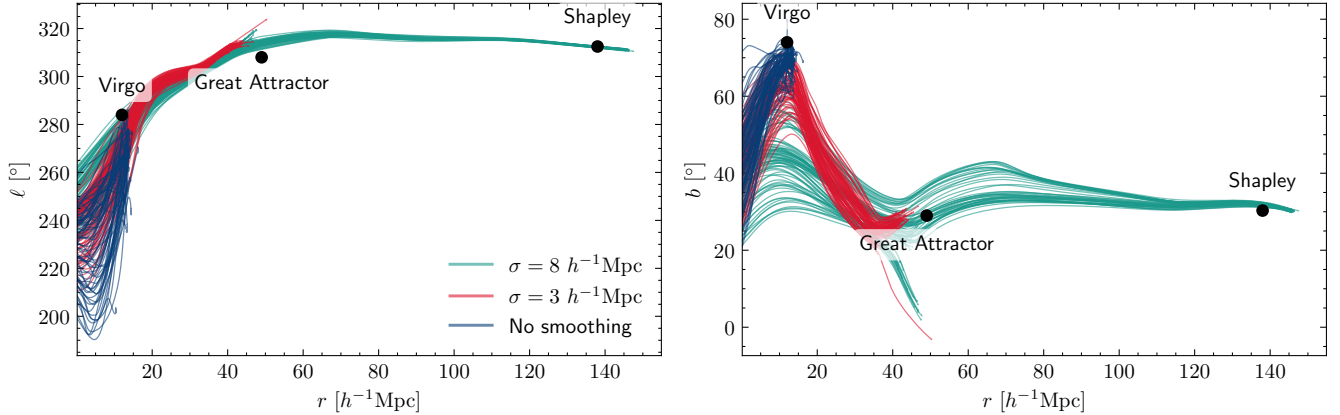


Figure 1 Milky Way streamline convergence points in Galactic coordinates for different smoothing scales applied to the **Manticore-Local** velocity fields. Left and right panels show the Galactic longitude and latitude as functions of distance from the observer, respectively. Colours represent different smoothing scales; each line shows the streamline from a single **Manticore-Local** realisation. Three discrete endpoints emerge: without smoothing, streamlines converge to Virgo; at $\sigma_{\text{smooth}} = 3 h^{-1} \text{Mpc}$ to the cGA; and at $\sigma_{\text{smooth}} = 8 h^{-1} \text{Mpc}$ to Shapley. Black points indicate the approximate positions of these structures, with the Classical *Great Attractor* position adopted from Dupuy *et al.* (2025).

TABLE 2
STREAMLINE GREAT ATTRACTOR CONVERGENCE COORDINATES OF
THE MILKY WAY STREAMLINE ACROSS GAUSSIAN SMOOTHING
SCALES.

$\sigma_{\text{smooth}} [h^{-1} \text{Mpc}]$	$r [h^{-1} \text{Mpc}]$	$\ell [\text{deg}]$	$b [\text{deg}]$
2	$41.0^{+2.0}_{-6.4}$	$313.0^{+1.4}_{-7.8}$	$27.3^{+1.4}_{-4.1}$
3	$41.3^{+2.0}_{-4.7}$	$313.0^{+1.1}_{-4.8}$	$27.4^{+1.8}_{-4.3}$
4	$41.8^{+1.5}_{-3.5}$	$312.0^{+1.3}_{-2.3}$	$26.7^{+2.3}_{-4.6}$

puted by Shaya *et al.* (2022). This is in good agreement with the recent result of Dupuy *et al.* (2025), who reported $(\ell, b) = (308.4 \pm 2.4 \text{ deg}, 29.0 \pm 1.9 \text{ deg})$ at a distance of $50 \pm 4 h^{-1} \text{Mpc}$.

In Fig. 2, we show the enclosed mass profile around the cGA convergence point at $\sigma_{\text{smooth}} = 3 h^{-1} \text{Mpc}$, i.e. the cGA inferred by **Manticore-Local**. The enclosed mass is obtained by summing voxel masses within radius r of the convergence point position, averaged over the **Manticore-Local** realisations. The profile shows a $2-3\sigma$ overdensity out to about $20 h^{-1} \text{Mpc}$. However, when we compare the enclosed mass profile directly with the nearby Centaurus cluster, we find that the cGA overdensity is similar. Furthermore, we compare the enclosed mass to that of Norma, which has been reported to be at the centre of the cGA (Woudt and Kraan-Korteweg 2000; Woudt *et al.* 2008) but which we shall find not to belong to the sGA basin. The enclosed mass profile around Norma is significantly larger up to about $10 h^{-1} \text{Mpc}$, reflecting not only its higher mass compared to Centaurus but also that both Norma and Centaurus pointings are centred directly on the haloes representing these clusters, whereas the cGA convergence point does not necessarily correspond to the centre of a massive halo.

We now characterise the basin associated with the cGA convergence point by selecting all voxels whose streamlines converge to the identified sGA position and computing the total enclosed mass and equivalent spherical radius. We find the total mass of all such voxels to be $\log(M/(h^{-1} M_{\odot})) = 16.4^{+0.1}_{-0.1}$, and the corresponding equivalent spherical radius is $R = 42^{+3}_{-1} h^{-1} \text{Mpc}$, though the basin is highly non-spherical (see Fig. 3). A sphere

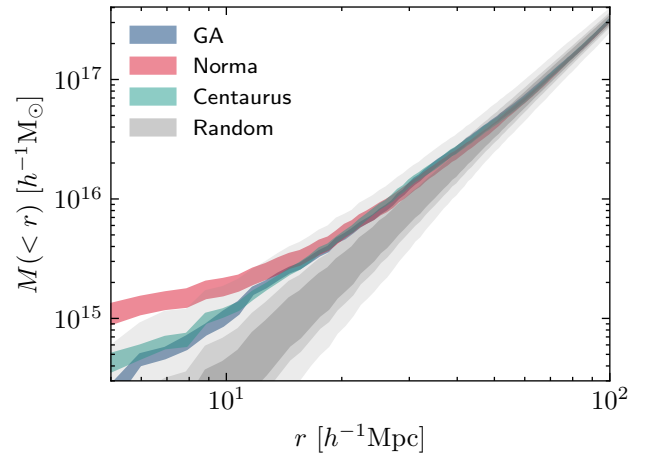


Figure 2 Enclosed mass profile around the **Manticore-Local** inferred Classical *Great Attractor* position at $(\ell, b) = (313^{+1}_{-5}, 27^{+2}_{-4}) \text{ deg}$ and distance $r = 41^{+2}_{-5} h^{-1} \text{Mpc}$ identified from the Milky Way streamline at $\sigma_{\text{smooth}} = 3 h^{-1} \text{Mpc}$, averaged over 80 **Manticore-Local** realisations. For comparison, we also show profiles centred on Norma, Centaurus, and random positions. The profile exhibits a $2-3\sigma$ overdensity out to $20 h^{-1} \text{Mpc}$, confirming a significant mass concentration at this location.

of this radius at the mean matter density ($\bar{\rho}_m = \Omega_m \rho_c$) would enclose the same mass, indicating that the over- and under-dense regions within the basin largely cancel.

Since the observer streamline converges to the cGA, we are located within this basin. In Fig. 3 we show the depth of the inferred cGA basin as a function of sky position in Galactic coordinates, computed by finding the distance to the farthest voxel whose streamline converges to the attractor for each sky direction. The basin extends to $\sim 80 h^{-1} \text{Mpc}$ in the direction of the convergence point (near the Centaurus and Hydra clusters) and only $\sim 13 h^{-1} \text{Mpc}$ in the opposite direction. A narrow protrusion of the cGA basin extends through the southern Galactic hemisphere from Fornax back toward the north, likely threading between the neighbouring Perseus-Pisces and Norma basins. Appendix A presents the standard deviation of the basin

depth across the 80 **Manticore-Local** realisations, together with the sky-projected mean density field. Across the 80 **Manticore-Local** realisations there is no tendency for another, comparably massive system to appear directly behind the ZoA. However, when testing **Manticore-Local** against the CosmicFlows-4 Tully-Fisher sample (Kourkchi *et al.* 2020), a residual external velocity $V_{\text{ext}} = 90 \pm 8 \text{ km s}^{-1}$ toward $(\ell, b) = (310 \pm 6, -5 \pm 4)$ deg remains, roughly aligned with the ZoA (McAlpine *et al.* 2025). This residual could indicate observational systematics, an unresolved structure within the reconstruction volume (e.g. in the ZoA), or the influence of mass beyond the ~ 200 Mpc covered by the 2M++ volume. We leave detailed investigation of this residual to future work with the BORG framework jointly analysing peculiar-velocity data in order to constrain the presence of massive structures behind the ZoA. Velocity-field-based reconstructions employing forward modelling of peculiar velocities (e.g. Valade *et al.* 2024) may be better at probing the mass distribution in obscured regions, since peculiar velocities are sensitive to larger scales. While Hollinger and Hudson (2024) quantified how rapidly linear-theory predictions based on 2M++ redshift data degrade in the ZoA, the extent to which BORG mitigates this degradation has not yet been tested, nor has a systematic comparison with velocity-field-based methods in these regions been carried out. We note, however, that because BORG infers a continuous Λ CDM realisation of the density field, it must smoothly interpolate between regions where data are available, placing implicit constraints on the ZoA. Our inferred cGA position already coincides well with that reported by Dupuy *et al.* (2025), who jointly analysed both redshift-space galaxy counts and peculiar velocities.

Of the galaxy clusters in our catalogue (Section 2.3), eight are members of the cGA basin in more than 50% of the **Manticore-Local** realisations, as determined by whether their reported positions lie within the basin. Hydra, Centaurus, Virgo, Abell 3565, Abell S0753, Fornax, and Ursa Major belong to the basin in all **Manticore-Local** realisations, whilst Abell 3574 is a member in 97% of the realisations. In contrast to previous studies, we find Norma (and Pavo II) to lie outside of the cGA basin. At low Galactic latitude, the Ophiuchus cluster (NeVe 1; $(\ell, b) \approx (1.3, 9.7)$ deg, $cz_{\text{CMB}} \approx 8550 \text{ km s}^{-1}$) is recovered by **Manticore-Local** as a halo of mass $\log(M_{200c}/(h^{-1} M_{\odot})) = 14.5^{+0.2}_{-0.3}$ at $(\ell, b) = (3.2^{+1.3}_{-1.8}, 10.6^{+1.0}_{-0.6})$ deg and $cz = 8810^{+140}_{-170} \text{ km s}^{-1}$, though at $|b| \approx 10$ deg it lies outside the effective 2M++ Galactic mask and is largely present in the input data.

4.2. Future dynamics analysis

We previously identified the GA as a convergence point of the present-day velocity field, but this construction reflects the instantaneous matter distribution, not the future dynamics. To determine which structures dominate the future displacement of the LG neighbourhood, we analyse the BPT suite of N -body simulations evolved from the **Manticore-Local** initial conditions to scale factor 10 (see Section 3.2).

We select particles within radius $R = 5 h^{-1} \text{ cMpc}$ of the observer position and track their evolution to $a = 10$. Choosing a larger radius would lead to enclosing parti-

cles close to the Virgo cluster, whose distance from the origin is $\sim 13 h^{-1} \text{ Mpc}$. In Fig. 4 we show the particle displacement magnitudes and directions in Galactic coordinates. Particles move on average towards the Virgo region but typically travel only $3 \pm 1 h^{-1} \text{ cMpc}$, well short of the $\sim 14 h^{-1} \text{ cMpc}$ separating Virgo from the box centre at $a = 10$. The displacement direction is $(\ell, b) = (232 \pm 51, 47 \pm 19)$ deg, broadly aligned with Virgo and with the LG velocity in the CMB frame (Planck Collaboration 2020), though shifted to somewhat lower longitude and latitude, reflecting the complex dynamics in this region. None of these particles become gravitationally bound to the Virgo halo by $a = 10$. Across the **Manticore-Local** realisations, the present-time observer velocity has mean $|v| = 457 \pm 56 \text{ km s}^{-1}$ at $(\ell, b) = (244 \pm 12, 39 \pm 10)$ deg, offset to lower longitude and latitude than the LG CMB-frame velocity of $\sim 620 \text{ km s}^{-1}$ towards $(272, 30)$ deg (Planck Collaboration 2020), consistent with the influence of Perseus and Fornax. However, the residual scatter of $\sim 150 \text{ km s}^{-1}$ from unresolved small-scale modes (below the BORG constraint scale) at galaxy-group scales complicates any stringent comparison between the BORG observer velocity and the LG CMB-frame velocity (Stiskalek *et al.* 2025). We consider the LG velocity further in Section 4.3. We verify that this conclusion holds even when evolving the simulations to $a = 100$. Examining the future displacement of the Virgo cluster itself in **Manticore-Local**, we find that at present its distance is $13^{+1}_{-1} h^{-1} \text{ cMpc}$ and its direction is $(\ell, b) = (287^{+4}_{-2}, 73^{+1}_{-1})$ deg. By $a = 10$, Virgo moves to $r = 14^{+1}_{-1} h^{-1} \text{ cMpc}$ and $(\ell, b) = (284^{+3}_{-4}, 67^{+1}_{-1})$ deg, suggesting a mild outward displacement in the direction of $(\ell, b) = (277^{+11}_{-14}, 19^{+11}_{-14})$ deg.

The streamlines from the Milky Way identify the cGA convergence point near the Abell 3565 cluster, which is represented in **Manticore-Local** at $a = 1$ by a halo of mass $\log(M_{200c}/(h^{-1} M_{\odot})) = 13.8^{+0.1}_{-0.2}$, although it appears in only 70% of the realisations. The other massive cluster close to this position is Abell S0753, with mass of $\log(M_{200c}/(h^{-1} M_{\odot})) = 14.0^{+0.1}_{-0.1}$, which is present in all **Manticore-Local** realisations. In realisations where both haloes are present at $a = 1$, they typically merge before $a = 10$, leading to a halo near the cGA position inferred from the streamlines, close to the present-time position of Abell 3565. When Abell 3565 is absent, the Abell S0753 halo generally migrates towards the cGA convergence point by $a = 10$.

Table 3 summarises the positions of the observed clusters near the cGA convergence point and their corresponding **Manticore-Local** present-time haloes, together with their halo masses and streamline-basin memberships. There is excellent agreement with the observed positions of all clusters. The other massive cluster near the cGA position is Centaurus, which in **Manticore-Local** has a mass of $\log(M_{200c}/(h^{-1} M_{\odot})) = 14.3^{+0.1}_{-0.1}$. By $a = 10$ it grows to $\log(M_{200c}/(h^{-1} M_{\odot})) = 14.4^{+0.1}_{-0.1}$ and undergoes only mild displacement, reaching $r = 35^{+1}_{-1} h^{-1} \text{ cMpc}$ and $(\ell, b) = (306^{+1}_{-1}, 24^{+1}_{-1})$ deg.

This indicates that Virgo, not the previously identified cGA convergence point, is the dominant (bound) structure determining the future LG displacement, with secondary contributions from other nearby massive clus-

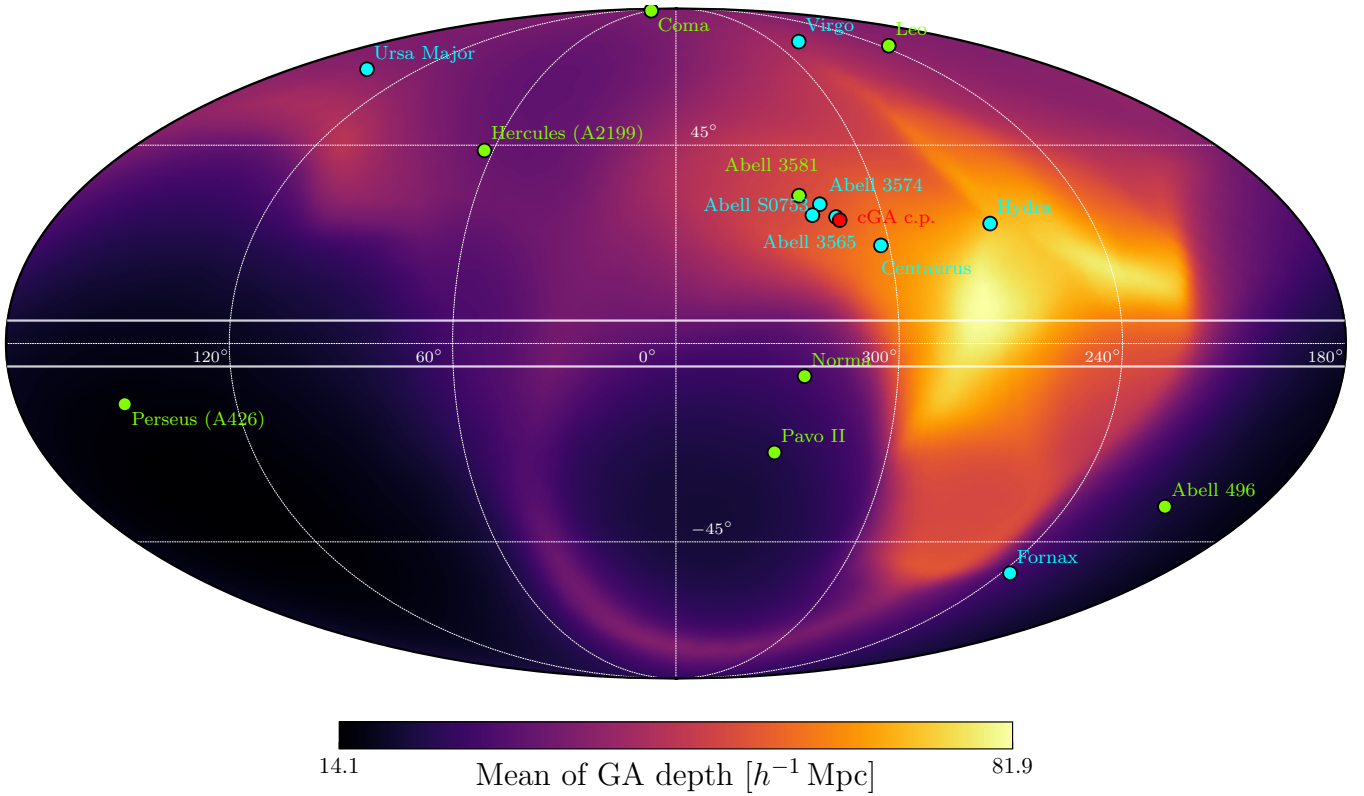


Figure 3 Depth of the inferred Classical *Great Attractor* basin as a function of sky position in Galactic coordinates, averaged over 80 *Manticore-Local* realisations. The basin is defined by selecting all voxels whose streamlines converge to the cGA position identified from the Milky Way streamline at $\sigma_{\text{smooth}} = 3 h^{-1} \text{Mpc}$, and “cGA c.p.” indicates its convergence point. For each sky direction, the depth is computed as the distance to the farthest voxel whose streamline converges to the cGA position. The basin is highly elongated, reaching six times farther toward the convergence point than away from it. Clusters that belong to the cGA basin in $> 50\%$ of the realisations are plotted in cyan, whilst other clusters from Table 1 within $100 h^{-1} \text{Mpc}$ are shown in green. The inferred cGA convergence point is also indicated in cyan; the ZoA (white lines at $b = \pm 45 \text{ deg}$) is shown for reference. Dashed white lines indicate meridians every 60 deg and parallels at $\pm 45 \text{ deg}$.

Dynamical Great Attractor: Future displacement towards Virgo

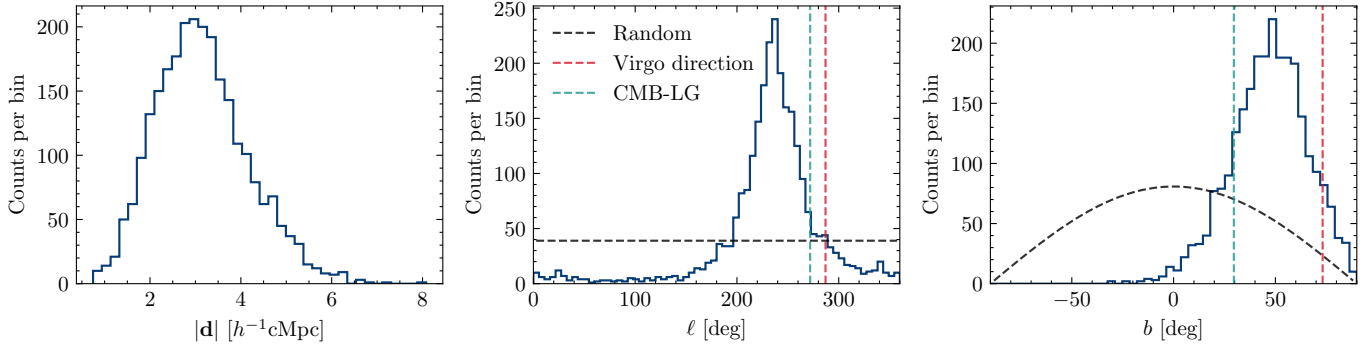


Figure 4 Displacement vectors of particles within $R = 5 h^{-1} \text{cMpc}$ of the observer position (centre of the box), tracked from $a = 1$ to $a = 10$, shown in Galactic coordinates (magnitude, longitude, and latitude, respectively) stacked over the simulations. Particles typically move towards the Virgo cluster but fall short of reaching it; Virgo’s distance from the box centre at $a = 10$ is approximately $14 h^{-1} \text{cMpc}$. Vertical lines mark Virgo at $(\ell, b) = (287.0, 73.2) \text{ deg}$ (red) and the LG CMB-frame velocity at $(\ell, b) = (271.9, 29.6) \text{ deg}$ (cyan) as reported by *Planck* ([Planck Collaboration 2020](#)). The ℓ and b panels show the expected isotropic distribution as black dashed lines.

ters as quantified in Table 4 and discussed below. Although there is a clear convergence point of the Milky Way streamlines, our dynamical analysis shows that the LG’s future displacement is directed towards Virgo as the dGA, not this intermediate-scale structure. In fact, this result agrees with the streamline analysis in Section 4.1: when no smoothing is applied to the velocity field, the observer streamline converges to Virgo.

Manticore-Local identifies Norma and Perseus as the most massive systems within 6000 km s^{-1} , with masses of $\log(M_{200c}/(h^{-1} M_{\odot})) = 14.8_{-0.1}^{+0.1}$ and $\log(M_{200c}/(h^{-1} M_{\odot})) = 14.9_{-0.1}^{+0.1}$, respectively (see Table 3). Neither cluster is part of the sGA basin in our streamline analysis (Section 4.1), likely because each forms its own basin of attraction. The next most massive cluster is Coma, although it lies farther away at $\sim 74 h^{-1} \text{ Mpc}$.

Finally, we assess the relative influence of nearby haloes using a simple illustrative model in which the Newtonian gravitational force on an observer at the box centre scales as $F \propto M_{200c}/r^2$. Importantly, individual clusters contribute only $\sim 10 \text{ km s}^{-1}$ to peculiar velocities; the bulk arises from integration over supercluster-scale matter distributions. Summing the contributions from bound haloes therefore falls well short of the observed $\sim 600 \text{ km s}^{-1}$, and this analysis serves only to illustrate the relative importance of nearby structures rather than to account for the full peculiar velocity budget; integration over all matter within a given radius is performed in Section 4.3. For each realisation we rank forces from all haloes on the observer, retain the top 100 contributors, and then stack these across realisations using the halo-association scheme of **McAlpine (2025)** to identify persistent contributors across the posterior. Table 4 lists the nine largest contributions from haloes within $155 h^{-1} \text{ Mpc}$, normalised to the strongest contributor and interpreted as the principal drivers of the future dGA direction. The dominant contribution arises from haloes representing Virgo, followed by Perseus at roughly 22% of Virgo’s influence, Fornax at a similar level (present in 88% of the realisations), Norma at about 17%, and Centaurus at about 13%. In approximately 25% of the realisations, a halo representing the nearby Ursa Major cluster (**Trentham et al. 2001**) appears and exerts a force comparable to that of Perseus, though with mass of $\log(M_{200c}/(h^{-1} M_{\odot})) \approx 13.5$ it sits near the resolution limit of our BPT suite (but not of the higher-resolution **Manticore-Local** main suite).

4.3. Explaining the Local Group velocity

In **Manticore-Local**, the present-day observer velocity has mean amplitude $|v| = 457 \pm 56 \text{ km s}^{-1}$ directed towards $(\ell, b) = (244 \pm 12, 39 \pm 10)$ deg, including the residual external velocity $V_{\text{ext}} = 90 \pm 8 \text{ km s}^{-1}$ inferred by comparing **Manticore-Local** to the CosmicFlows-4 Tully–Fisher sample (**Kourkchi et al. 2020**). This is both lower in amplitude and offset in direction from the LG velocity in the CMB frame of $\sim 620 \text{ km s}^{-1}$ towards $(272, 30)$ deg (**Planck Collaboration 2020**).

Since **Lynden-Bell et al. (1988)** originally invoked the GA to explain the LG velocity in the CMB frame, we now assess which scales contribute to the LG velocity within **Manticore-Local**, following **Lavaux et al.**

(2010). **Lavaux et al. (2010)** reconstructed the local velocity field using the 2MASS galaxy catalogue and found that structures within $40 h^{-1} \text{ Mpc}$ of the LG contribute approximately half the CMB dipole amplitude. They found no convergence in either amplitude or sky direction even at scales of $150 h^{-1} \text{ Mpc}$; mass within this distance yields a dipole of $500 \pm 100 \text{ km s}^{-1}$, offset in direction by $40\text{--}50$ deg. These findings are consistent with **Manticore-Local**, which similarly exhibits a lower LG dipole amplitude and a directional offset. Using linear theory applied to the 2M++ compilation, **Carrick et al. (2015)** predicted a LG velocity of $540 \pm 40 \text{ km s}^{-1}$ towards $(\ell, b) = (268 \pm 4, 38 \pm 6)$ deg, only 10 deg from the CMB dipole direction. Nevertheless, they found a need for an external bulk flow of $159 \pm 23 \text{ km s}^{-1}$ towards $(\ell, b) = (304 \pm 11, 6 \pm 13)$ deg at 5.1σ significance, indicating that sources beyond $\sim 200 h^{-1} \text{ Mpc}$ (or in the ZoA) still contribute appreciably.

In Fig. 5, we examine which scales contribute to the **Manticore-Local** observer velocity by applying the linear theory expression of eq. (1) to compute the velocity sourced by matter within radius R . Consistent with **Lavaux et al. (2010)**, mass within $40 h^{-1} \text{ Mpc}$ contributes approximately half the LG velocity amplitude, broadly in line with the decomposition of **Tully et al. (2008)**, who attributed 259 km s^{-1} to evacuation from the Local Void, 185 km s^{-1} to the Virgo cluster and its surroundings, and 455 km s^{-1} toward Centaurus from scales beyond 3000 km s^{-1} . Even when including mass out to $155 h^{-1} \text{ Mpc}$ (the approximate extent of the **Manticore-Local** reconstruction volume), we recover only $72 \pm 9\%$ of the CMB dipole amplitude, with the direction remaining offset by 38 ± 10 deg. Computing the velocity sourced specifically by mass within the cGA basin (which is highly asymmetric around the observer; see Fig. 3), we find $|V_{\text{cGA}}| = 324 \pm 51 \text{ km s}^{-1}$ towards $(\ell, b) = (243 \pm 20, 57 \pm 11)$ deg. This corresponds to $\sim 75\%$ of the total observer velocity amplitude, but the direction differs by ~ 20 deg from the final velocity; mass beyond the basin is therefore required not only to increase the amplitude but also to rotate the velocity vector. Structures beyond the cGA basin contribute significantly, with potentially substantial contributions from mass beyond the **Manticore-Local** volume.

Two explanations may account for this discrepancy. First, the measured CMB dipole arises from the non-linear velocity field, whereas **Manticore-Local** captures only mildly non-linear scales. Following **Stiskalek et al. (2025)**, the residual velocity scatter between **BORG** reconstructions and peculiar velocity data is typically $\sim 150 \text{ km s}^{-1}$; incorporating this scatter reduces the discrepancy to an insignificant 1σ disagreement, as shown in Fig. 5. However, this argument is disfavoured by the observation that all galaxies within the Local Sheet ($\lesssim 5 h^{-1} \text{ Mpc}$) share essentially the same velocity as the LG (**Tully et al. 2008**), implying that the local flow field is dynamically cold and that the LG velocity has no significant non-linear component. Second, mass beyond $\sim 150 h^{-1} \text{ Mpc}$ (the **Manticore-Local** reconstruction volume), or in the ZoA, may contribute significantly to the LG velocity (**Peacock 1992**).

To test the second hypothesis, we analyse the 15,000 random Quijote simulations described in Section 2.2.

TABLE 3
COMPARISON OF OBSERVED POSITIONS (TABLE 1) WITH MANTICORE-LOCAL HALO PROPERTIES AT $a = 1$ FOR SELECTED GALAXY CLUSTERS IN THE GA REGION. COORDINATES ARE GIVEN IN GALACTIC COORDINATES AND CLUSTERS ARE ORDERED BY THEIR OBSERVED REDSHIFT.

Name	Observed			Manticore-Local				
	ℓ [deg]	b [deg]	cz_{CMB} [km s $^{-1}$]	ℓ [deg]	b [deg]	r [h^{-1} cMpc]	$\log M_{200c}$ [$h^{-1} M_{\odot}$]	cGA member
Inferred cGA	–	–	–	313.0 $^{+1.1}_{-4.8}$	27.4 $^{+1.8}_{-4.3}$	41.3 $^{+2.0}_{-4.7}$	–	–
Ursa Major	144.6	65.5	1101	147.3 $^{+8.9}_{-6.3}$	70.7 $^{+2.7}_{-9.2}$	11.8 $^{+1.8}_{-2.8}$	13.6 $^{+0.1}_{-0.3}$	100%
Fornax	236.7	–53.0	1332	235.6 $^{+6.5}_{-5.1}$	–53.5 $^{+1.9}_{-1.2}$	13.5 $^{+1.3}_{-1.1}$	13.8 $^{+0.2}_{-0.2}$	100%
Virgo	283.8	74.4	1636	287.0 $^{+4.2}_{-1.5}$	73.2 $^{+1.4}_{-1.4}$	13.0 $^{+0.9}_{-0.5}$	14.4 $^{+0.1}_{-0.1}$	100%
Centaurus	302.4	21.6	3403	303.0 $^{+0.4}_{-0.7}$	21.7 $^{+0.6}_{-0.5}$	34.1 $^{+0.8}_{-0.8}$	14.3 $^{+0.1}_{-0.1}$	100%
Hydra	269.6	26.5	4058	269.6 $^{+0.3}_{-0.3}$	26.5 $^{+0.4}_{-0.4}$	43.5 $^{+1.1}_{-1.2}$	14.3 $^{+0.1}_{-0.1}$	100%
Abell 3565	313.5	28.0	4120	313.5 $^{+1.4}_{-1.1}$	29.0 $^{+0.9}_{-0.7}$	40.8 $^{+1.6}_{-1.0}$	13.8 $^{+0.1}_{-0.2}$	100%
Abell S0753	320.3	28.4	4200	319.5 $^{+0.6}_{-1.6}$	26.5 $^{+1.0}_{-0.5}$	42.9 $^{+1.3}_{-1.0}$	14.0 $^{+0.1}_{-0.1}$	100%
Abell 3574	317.5	30.9	4942	317.6 $^{+0.6}_{-0.5}$	31.5 $^{+0.4}_{-0.4}$	50.6 $^{+1.4}_{-1.6}$	13.9 $^{+0.2}_{-0.2}$	97%
Norma	325.3	–7.1	4955	325.3 $^{+0.4}_{-0.3}$	–6.3 $^{+0.4}_{-0.4}$	51.0 $^{+1.1}_{-0.8}$	14.8 $^{+0.1}_{-0.1}$	No
Perseus	150.6	–13.3	4995	150.3 $^{+0.4}_{-0.4}$	–13.5 $^{+0.3}_{-0.2}$	51.5 $^{+1.1}_{-2.2}$	14.9 $^{+0.1}_{-0.1}$	No

TABLE 4
MOST INFLUENTIAL HALOES CONTRIBUTING TO THE GRAVITATIONAL FORCE ON THE OBSERVER, RANKED BY $F \propto M_{200c}/r^2$ AND NORMALISED TO THE STRONGEST CONTRIBUTOR. POSITIONS AND DISTANCES ARE AVERAGED OVER THE MANTICORE-LOCAL REALISATIONS IN WHICH EACH HALO IS PRESENT; COUNT IS THE NUMBER OF REALISATIONS (OUT OF 50) CONTAINING THE HALO.

Name	Count	r [h^{-1} cMpc]	F/F_{max}
Virgo	50	13.18	1.0
Perseus	50	51.18	0.22
Fornax	44	14.45	0.22
Ursa Major	13	12.61	0.17
Norma	50	51.15	0.17
Centaurus	47	34.09	0.13
Coma	49	72.20	0.10
Pavo II	38	44.48	0.10
Antlia	21	30.96	0.10

For each simulation, we extract the linear velocity of an observer at the box centre, \mathbf{V}_{box} , and compute the velocity sourced by matter within radius R , $\mathbf{V}_{\text{inner}}(R)$. Fig. 6 shows the distribution of $|\mathbf{V}_{\text{box}}|$ across all simulations; the observed LG velocity lies well within the bulk of the distribution, indicating that such velocities are typical in Λ CDM. In Fig. 7, we select observers with $|\mathbf{V}_{\text{box}}|$ between 560 and 680 km s $^{-1}$, corresponding to the observed LG velocity in the CMB frame of 620 ± 15 km s $^{-1}$ (Planck Collaboration 2020) at 4σ ; this yields 1,882 observers out of 15,000 (12.5%). We show the amplitude ratio $|\mathbf{V}_{\text{inner}}(R)|/|\mathbf{V}_{\text{box}}|$ and the angle between the two vectors (the normalised dot product $\mathbf{V}_{\text{inner}}(R) \cdot \mathbf{V}_{\text{box}}/|\mathbf{V}_{\text{box}}|^2$ follows a nearly identical trend to the amplitude ratio and is omitted for brevity). We present results for two cases: pure linear velocities, and velocities with 150 km s $^{-1}$ noise added to \mathbf{V}_{box} to mimic non-linear contributions to the CMB dipole.

For pure linear velocities at $R = 150 h^{-1}$ Mpc, we find $|\mathbf{V}_{\text{inner}}|/|\mathbf{V}_{\text{box}}| = 0.93^{+0.12}_{-0.13}$ and an alignment angle of $\theta = 9.2^{+5.8}_{-4.6}$ deg. Although most of the observer velocity is typically sourced within this radius, notable outliers exist and misalignment can reach ~ 10 deg. Crucially, upon adding 150 km s $^{-1}$ uncertainty to \mathbf{V}_{box} , we find at $R = 150 h^{-1}$ Mpc that $|\mathbf{V}_{\text{inner}}|/|\mathbf{V}_{\text{box}}| = 0.87^{+0.30}_{-0.18}$ and an alignment angle of $\theta = 19.1^{+12.7}_{-9.9}$ deg. This scenario bet-

ter represents actual observations, where the measured CMB dipole contains non-linear contributions whilst the matter dipole is reconstructed only to mildly non-linear scales. The Manticore-Local results are therefore consistent with the observed LG velocity in the CMB frame at the $\sim 1\sigma$ level.

We quantify this agreement more directly in Fig. 8, which shows the joint distribution of magnitude ratio and angular misalignment for both Manticore-Local and the random Quijote simulations. The magnitude ratio is defined as the amplitude of the velocity sourced by matter within 155 h^{-1} Mpc divided by a reference velocity, while the angular misalignment is the angle between these two vectors. The reference velocity is taken to be the CMB dipole for Manticore-Local and the full-box velocity for Quijote; a direct comparison therefore assumes that the full velocity of a central observer in the cosmic rest frame is generated entirely within the Quijote volume. Without small-scale velocity scatter σ_v , Manticore-Local is discrepant with the random simulations at 2.0σ significance, computed using the posterior agreement metric.⁴ This suggests that even including mass beyond the Manticore-Local reconstruction volume is unlikely to fully reconcile the predicted and observed LG velocities from linear theory alone. However, upon adding $\sigma_v = 150$ km s $^{-1}$ scatter (representing small-scale, non-linear contributions to the observer velocity below the BORG resolution), the discrepancy reduces to 0.5σ .

5. DISCUSSION & CONCLUSION

In this paper we examine the GA using three complementary approaches: present-day streamline reconstruction (the traditional method yielding the cGA), future gravitational evolution with Manticore-Local digital twins built with the BORG algorithm yielding the dGA, and an assessment within Manticore-Local of which scales source the LG velocity in the CMB frame. Dressler *et al.* (1987) fitted a bulk flow from elliptical-galaxy peculiar velocities and noted that Hydra–Centaurus itself was moving toward mass beyond ~ 5000 km s $^{-1}$; Lynden-Bell *et al.* (1988) then fitted an attractor model, identifying the GA at $(\ell, b) \approx (307, 9)$ deg and $cz \approx 4350$ km s $^{-1}$ with inferred mass $\sim 5.4 \times 10^{16} M_{\odot}$. Recent

⁴ <https://github.com/SebastianBocquet/PosteriorAgreement>

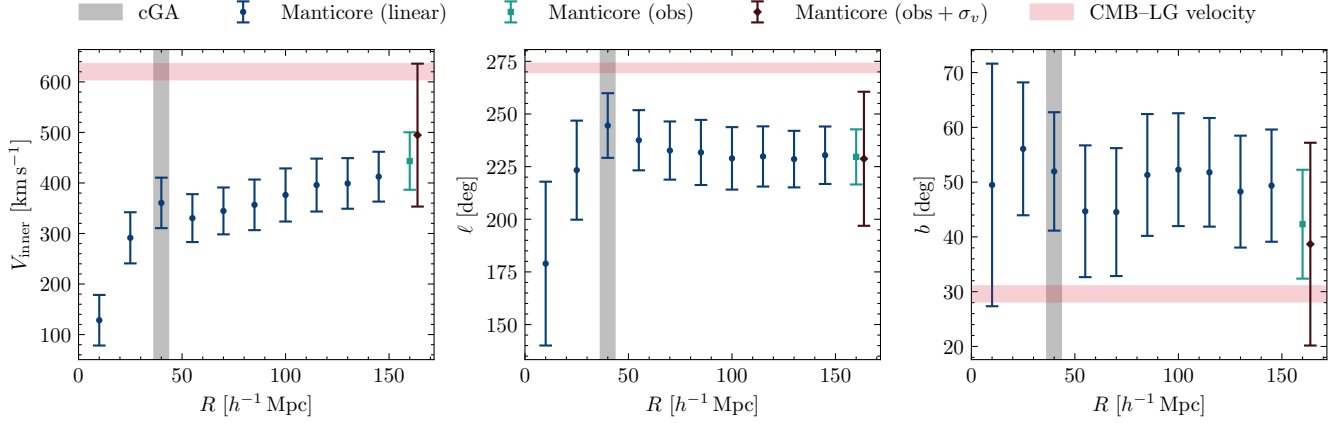


Figure 5 Observer velocity sourced by matter within radius R in **Manticore-Local**. *Left*: Amplitude $|\mathbf{V}_{\text{inner}}(R)|$. *Centre*: Galactic longitude ℓ of $\mathbf{V}_{\text{inner}}(R)$. *Right*: Galactic latitude b of $\mathbf{V}_{\text{inner}}(R)$. “**Manticore (linear)**” shows the linear velocity sourced by matter within radius R , computed using eq. (1). “**Manticore (obs)**” denotes the observer velocity computed from the entire **Manticore-Local** simulation box, including the external velocity dipole of $90 \pm 8 \text{ km s}^{-1}$. “**Manticore (obs + σ_v)**” includes 150 km s^{-1} scatter to mimic non-linear contributions. Horizontal red bands indicate the observed LG velocity in the CMB frame ([Planck Collaboration 2020](#)). Vertical grey bands indicate the 16th–84th percentile on the inferred distance to the cGA convergence point in **Manticore-Local**; mass within the cGA basin contributes $\sim 75\%$ of the observer velocity amplitude, but the direction at this radius differs from the final direction by ~ 20 deg, requiring contributions from larger scales to rotate the velocity vector. All error bars and shaded regions show 1σ uncertainties. The “**Manticore (obs)**” and “**Manticore (obs + σ_v)**” markers are offset horizontally for visual clarity.

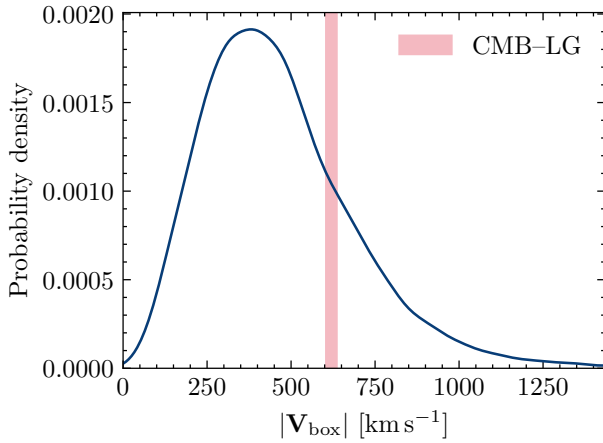


Figure 6 Distribution of observer velocity amplitudes $|\mathbf{V}_{\text{box}}|$ across the 15,000 fiducial-cosmology **Quijote** simulations ([Villaescusa-Navarro et al. 2020](#)). Velocities are computed assuming linear theory (eq. (1)) for observers located at the box centre. The vertical red band indicates the observed LG velocity in the CMB frame of $620 \pm 15 \text{ km s}^{-1}$ (1σ). The LG velocity is consistent with typical Λ CDM expectations.

peculiar-velocity samples ([Tully et al. 2014](#); [Dupuy and Courtois 2023](#)) motivated streamline-based basin definitions ([Dupuy et al. 2019, 2020](#)), with [Dupuy et al. \(2025\)](#) locating the cGA at $(\ell, b) = (308.4 \pm 2.4 \text{ deg}, 29.0 \pm 1.9 \text{ deg})$ and $50 \pm 4 \text{ h}^{-1} \text{ Mpc}$ via a joint machine-learning analysis combining redshift-space counts and peculiar velocities.

Applying the streamline method to **Manticore-Local** at $\sigma_{\text{smooth}} = 3 \text{ h}^{-1} \text{ Mpc}$, we locate the cGA convergence point at $(\ell, b) = (313_{-5}^{+1}, 27_{-4}^{+2}) \text{ deg}$ and $41_{-5}^{+2} \text{ h}^{-1} \text{ Mpc}$, close to Abell 3565 within the Hydra-Centaurus supercluster. The mass of the associated basin is $\log(M/(h^{-1} M_{\odot})) = 16.4_{-0.1}^{+0.1}$ (Table 2). Hydra, Virgo, and Abell 3574 are cGA basin members in most **Manticore-Local** realisations, and the basin

depth is asymmetric (Fig. 3). Crucially, Fig. 1 shows that the streamline-defined convergence point shifts with smoothing: negligible smoothing yields Virgo, intermediate smoothing the cGA, and large smoothing Shapley, underscoring the construct’s ambiguity. Abell 3565 and Abell S0753 counterparts typically merge by $a = 10$, while Centaurus remains near its present position. We summarise the **Manticore-Local** counterparts to these observed clusters in Table 3. Norma, though massive, is not part of the cGA but rather generally forms its own basin.

Evolving the **Manticore-Local** realisations to $a = 10$ from the present in the BPT suite (corresponding to a Universe age of 52.4 Gyr), particles within $5 \text{ h}^{-1} \text{ cMpc}$ of the observer drift only $3 \pm 1 \text{ h}^{-1} \text{ cMpc}$ toward Virgo, remaining unbound; simulating to the scale factor of 100 changes nothing because accelerated expansion halts further structure growth (Fig. 4). Virgo itself shifts modestly to $r \approx 14 \text{ h}^{-1} \text{ cMpc}$ and $(\ell, b) \approx (284, 67) \text{ deg}$ by $a = 10$. We find that Virgo dominates the gravitational pull on the observer, defining the future *dynamical GA* direction, with Perseus, Fornax, Ursa Major, and Norma contributing at roughly one-fifth of Virgo’s level, and Centaurus at $\sim 13\%$ (Table 4). However, particles from the observer position never actually reach Virgo; they travel only $\sim 3 \text{ h}^{-1} \text{ cMpc}$ whilst Virgo remains $\sim 14 \text{ h}^{-1} \text{ cMpc}$ away at $a = 10$, with dark energy domination within the assumed flat Λ CDM cosmology preventing further gravitational collapse.

Addressing the original motivation of [Lynden-Bell et al. \(1988\)](#)—whether the cGA sources the LG peculiar velocity—we find that mass within $155 \text{ h}^{-1} \text{ Mpc}$ (the extent of the **Manticore-Local** reconstruction volume) accounts for only $72 \pm 9\%$ of the CMB dipole amplitude, with the direction offset by $38 \pm 10 \text{ deg}$. Using random Λ CDM simulations, we show that this incomplete convergence is consistent with expectations: considering the velocity sourced by matter within radius R , observers with LG-like velocities receive $93 \pm 12\%$ of their total

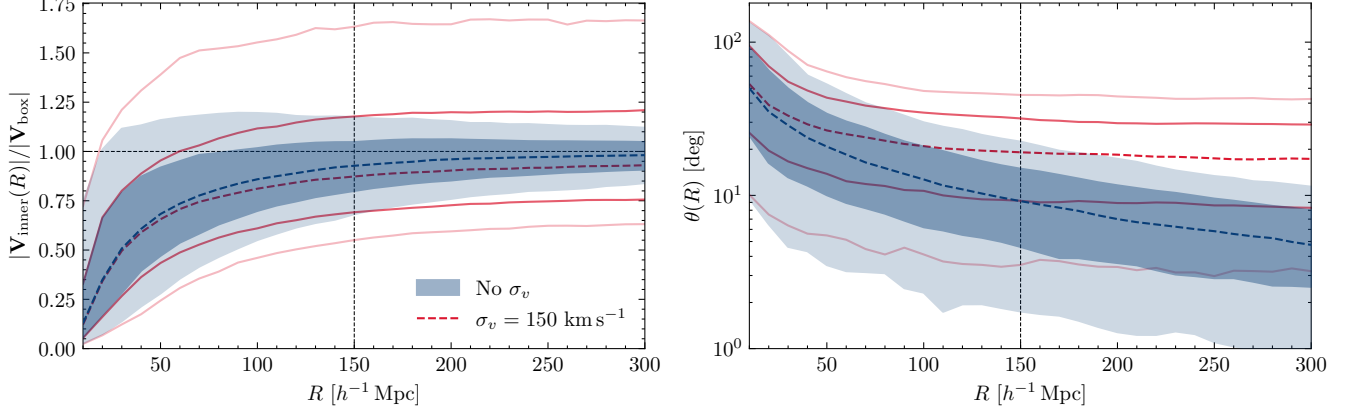


Figure 7 Convergence of observer velocity with reconstruction radius in random Λ CDM simulations. We use these simulations to test whether the incomplete convergence of **Manticore-Local** observer velocities at $155 h^{-1}$ Mpc is consistent with Λ CDM expectations for the contribution of mass beyond the reconstruction volume. Statistics are computed for observers with $|\mathbf{V}_{\text{box}}|$ between 560 and 680 km s^{-1} , corresponding to the observed LG velocity in the CMB frame of $620 \pm 15 \text{ km s}^{-1}$ at 4σ . *Left*: Normalised dot product $\mathbf{V}_{\text{inner}}(R) \cdot \mathbf{V}_{\text{box}} / (|\mathbf{V}_{\text{inner}}(R)| |\mathbf{V}_{\text{box}}|)$. *Centre*: Amplitude ratio $|\mathbf{V}_{\text{inner}}(R)| / |\mathbf{V}_{\text{box}}|$. *Right*: Alignment angle between $\mathbf{V}_{\text{inner}}(R)$ and \mathbf{V}_{box} . Bands show 1σ and 2σ confidence regions, with blue for pure linear velocities and red including 150 km s^{-1} scatter propagated to \mathbf{V}_{box} to mimic non-linear contributions. At $R = 150 h^{-1}$ Mpc, with scatter included, typical observers recover $\sim 87\%$ of their total velocity amplitude with ~ 19 deg misalignment, demonstrating that the **Manticore-Local** results are consistent with Λ CDM expectations.

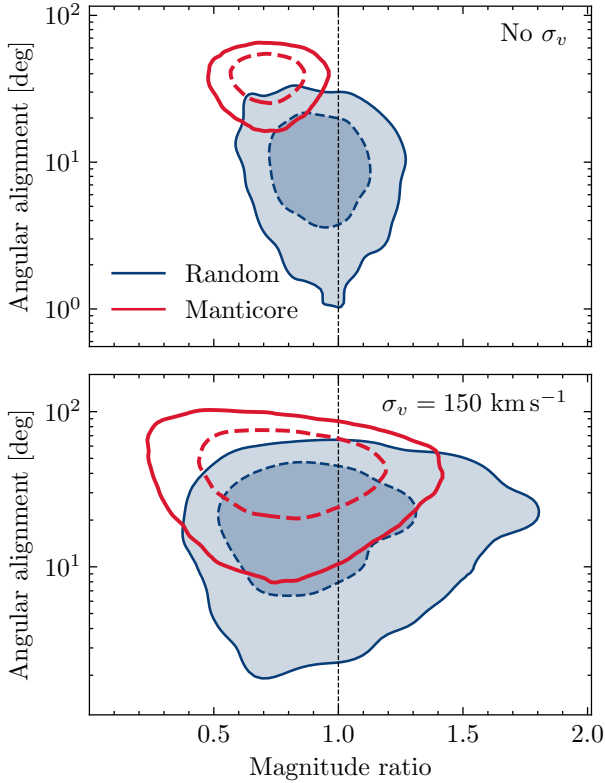


Figure 8 Joint distribution of magnitude ratio (velocity amplitude sourced within $155 h^{-1}$ Mpc divided by reference velocity) and angular misalignment for **Manticore-Local** (red contours) and random **Quijote** simulations (blue filled contours). For **Manticore-Local**, the reference velocity is the observed CMB dipole; for **Quijote**, it is the full-box velocity. Contours enclose 68% and 95% of the probability mass. *Top*: Without small-scale velocity scatter σ_v , where **Manticore-Local** is discrepant with random expectations at 2.0σ significance. *Bottom*: Including $\sigma_v = 150 \text{ km s}^{-1}$ scatter to account for non-linear contributions below the **BORG** resolution, reducing the discrepancy to 0.5σ .

velocity amplitude with 9.2 ± 5 deg misalignment from sources within $R = 150 h^{-1}$ Mpc for pure linear velocities. Upon adding 150 km s^{-1} scatter to mimic non-linear contributions to the CMB dipole, the amplitude ratio becomes $87^{+30}_{-18}\%$ with $19.1^{+12.7}_{-9.9}$ deg misalignment. Directly comparing **Manticore-Local** to the random simulations in the joint space of magnitude ratio and angular misalignment, the discrepancy is 2.0σ without small-scale velocity scatter σ_v , reducing to 0.5σ upon adding $\sigma_v = 150 \text{ km s}^{-1}$.

It is therefore not possible to identify the origin of the LG velocity from linear or mildly non-linear reconstructions of the local Universe, and nor is it expected to be (Peacock 1992). This is due to (i) mass beyond the **Manticore-Local** reconstruction volume, which deeper **BORG** reconstructions extending beyond the **2M++** could constrain, and (ii) small-scale non-linear motions below the **BORG** resolution, since comparisons between linear and non-linear velocity fields typically yield $\sim 150 \text{ km s}^{-1}$ scatter (Carrick et al. 2015), and the LG itself (with total mass $\sim 3 \times 10^{12} M_{\odot}$; Benisty et al. 2022; Wempe et al. 2024) lies well below the **BORG** constraint scale. Higher-resolution simulations of the immediate LG neighbourhood, such as the **BORG**-based reconstructions of Wempe et al. (2024, 2025), could help to quantify the non-linear contribution.

In summary, a cGA convergence point appears in present-day streamlines but only at intermediate smoothing. Furthermore, the cGA does not determine the LG’s future displacement direction; among bound structures, Virgo dominates, with other clusters contributing at only 10–20% of its influence, and the LG never reaches Virgo unless physics beyond Λ CDM alters the expansion history. Addressing the original question of what structures source the $\sim 600 \text{ km s}^{-1}$ CMB dipole, mass within $155 h^{-1}$ Mpc recovers only $\sim 72\%$ of the amplitude with ~ 38 deg directional offset; the Virgo supercluster alone contributes only $\sim 200 \text{ km s}^{-1}$, with the remainder arising from integration over larger scales (Section 4.3). Mass within the asymmetric cGA basin

contributes $\sim 75\%$ of the observer’s linear velocity amplitude, though the direction at this radius is offset by ~ 20 deg from the final velocity, with matter beyond the basin required to rotate the velocity vector.

These conclusions rest on the **Manticore-Local** realisations, the adopted smoothing and resolution, and the assumption of a flat Λ CDM cosmology. It is remarkable that **Manticore-Local** realisations provide counterpart haloes for nearly all observed clusters in the GA basin, including nearby lower-mass systems such as Fornax and Ursa Major, demonstrating the power of **BORG**-enabled digital twins for high-fidelity studies of the local Universe. These simulations accurately reproduce the cGA convergence point and allow us to pinpoint its location and the cluster population of its basin, showing that although it is a substantial overdensity it is not as overdense as the region surrounding the Norma and Perseus clusters. They also reveal that Norma is not a member of the streamline basin and that the cGA does not dominate the future dynamics of the LG. The streamline convergence point is thus a scale-dependent property of the instantaneous velocity field rather than a unique physical structure, and does not explain the local dynamics. With perfect knowledge of the velocity field, a unique set of basins of attraction, each with its own sink, would in principle be well defined. In practice, however, any finite-resolution reconstruction smooths over small-scale structure, merging smaller basins and their sinks into larger ones and making smoothing-scale-dependence unavoidable. Moreover, when dark energy becomes dominant and perturbation growth freezes, present-day streamlines become particularly poor tracers of future trajectories.

We therefore conclude that: (i) Virgo dominates the Local Group’s immediate dynamical evolution; (ii) the Classical *Great Attractor* represents a moderate overdensity embedded within a multiscale flow; and (iii) addressing the original motivation of the GA—explaining the CMB dipole—the LG velocity is sourced by structures across a wide range of scales, with even the linear contribution not guaranteed to converge within the $\sim 150 h^{-1}$ Mpc volume probed here, and the remaining

discrepancy likely arising from mass beyond this volume and small-scale non-linear motions. The **BORG** methodology of inferring initial conditions via Bayesian field-level reconstruction and evolving them beyond the present opens new avenues for understanding cosmic dynamics and could be extended to joint analyses with peculiar-velocity data to further constrain structures behind the ZoA, and more generally to understand both the density and velocity fields of the local Universe.

ACKNOWLEDGMENTS

We thank Pedro Ferreira for useful inputs and discussions.

RS acknowledges financial support from STFC Grant No. ST/X508664/1 and the Snell Exhibition of Balliol College, Oxford. HD is supported by a Royal Society University Research Fellowship (grant no. 211046). JJ acknowledges support from the research project *Understanding the Dynamic Universe*, funded by the Knut and Alice Wallenberg Foundation (Dnr KAW 2018.0067). JJ acknowledges the hospitality of the Aspen Center for Physics, which is supported by National Science Foundation grant PHY-1607611, and support for participation at the Aspen Center provided by the Simons Foundation. JJ acknowledges support from the Swedish Research Council (VR) under project 2020-05143, *Deciphering the Dynamics of Cosmic Structure*. GL, JJ, and SM acknowledge support from the Simons Foundation through the Simons Collaboration on “Learning the Universe”. GL acknowledges support from the CNRS IEA programme “Manticore”. MJH acknowledges support from an NSERC Discovery grant.

This work was done within the Aquila Consortium⁵. The authors would like to acknowledge the use of the University of Oxford Advanced Research Computing (ARC) facility in carrying out this work⁶. This research has made use of the NASA/IPAC Extragalactic Database (NED), which is operated by the Jet Propulsion Laboratory, California Institute of Technology, under contract with the National Aeronautics and Space Administration.

REFERENCES

- P. B. Lilje, A. Yahil, and B. J. T. Jones, *ApJ* **307**, 91 (1986).
 D. Lynden-Bell, S. M. Faber, D. Burstein, R. L. Davies, A. Dressler, R. J. Terlevich, and G. Wegner, *ApJ* **326**, 19 (1988).
 D. Pomarède, Y. Hoffman, H. M. Courtois, and R. B. Tully, *ApJ* **845**, 55 (2017), [arXiv:1706.03413 \[astro-ph.CO\]](https://arxiv.org/abs/1706.03413).
 R. C. Kraan-Korteweg, M. E. Cluver, M. Bilicki, T. H. Jarrett, M. Colless, A. Elagali, H. Böhringer, and G. Chon, *MNRAS* **466**, L29 (2017), [arXiv:1611.04615 \[astro-ph.CO\]](https://arxiv.org/abs/1611.04615).
 H. M. Courtois, R. C. Kraan-Korteweg, A. Dupuy, R. Graziani, and N. I. Libeskind, *MNRAS* **490**, L57 (2019), [arXiv:1909.08875 \[astro-ph.CO\]](https://arxiv.org/abs/1909.08875).
 D. Pomarède, R. B. Tully, R. Graziani, H. M. Courtois, Y. Hoffman, and J. Lezmy, *ApJ* **897**, 133 (2020), [arXiv:2007.04414 \[astro-ph.CO\]](https://arxiv.org/abs/2007.04414).
 G. F. Smoot, M. V. Gorenstein, and R. A. Muller, *Phys. Rev. Lett.* **39**, 898 (1977).
 A. Dressler, S. M. Faber, D. Burstein, R. L. Davies, D. Lynden-Bell, R. J. Terlevich, and G. Wegner, *ApJ* **313**, L37 (1987).
 M. Aaronson, J. Huchra, J. Mould, P. L. Schechter, and R. B. Tully, *ApJ* **258**, 64 (1982).
 M. J. Hudson, *MNRAS* **265**, 43 (1993a).
 M. J. Hudson, *MNRAS* **265**, 72 (1993b).
 M. J. Hudson, *MNRAS* **266**, 475 (1994a).
 R. W. Pike and M. J. Hudson, *ApJ* **635**, 11 (2005), [arXiv:astro-ph/0511012 \[astro-ph\]](https://arxiv.org/abs/astro-ph/0511012).
 J. Carrick, S. J. Turnbull, G. Lavaux, and M. J. Hudson, *MNRAS* **450**, 317 (2015), [arXiv:1504.04627 \[astro-ph.CO\]](https://arxiv.org/abs/1504.04627).
 J. Jasche and G. Lavaux, *A&A* **625**, A64 (2019), [arXiv:1806.11117 \[astro-ph.CO\]](https://arxiv.org/abs/1806.11117).
 A. Dressler and S. M. Faber, *ApJ* **354**, 13 (1990a).
 A. Dressler and S. M. Faber, *ApJ* **354**, L45 (1990b).
 D. Burstein, S. M. Faber, and A. Dressler, *ApJ* **354**, 18 (1990).
 M. J. Hudson, *MNRAS* **266**, 468 (1994b).
 E. Bertschinger and R. Juszkiewicz, *ApJ* **334**, L59 (1988).
 R. C. Kraan-Korteweg, P. A. Woudt, V. Cayatte, A. P. Fairall, C. Balkowski, and P. A. Henning, *Nature* **379**, 519 (1996).
 P. A. Woudt, R. C. Kraan-Korteweg, J. Lucey, A. P. Fairall, and S. A. W. Moore, *MNRAS* **383**, 445 (2008), [arXiv:0706.2227 \[astro-ph\]](https://arxiv.org/abs/0706.2227).

⁵ <https://aquila-consortium.org>

⁶ <https://doi.org/10.5281/zenodo.22558>

- N. Hatamkhani, R. C. Kraan-Korteweg, S. L. Blyth, K. Said, and A. Elagali, *MNRAS* **522**, 2223 (2023), arXiv:2304.07208 [astro-ph.GA].
- S. H. A. Rajohnson, R. C. Kraan-Korteweg, B. S. Frank, H. Chen, L. Staveley-Smith, P. Serra, N. Steyn, S. Kurapati, D. J. Pisano, and S. Goedhart, *MNRAS* **535**, 3429 (2024), arXiv:2411.07084 [astro-ph.GA].
- R. Scaramella, G. Baiesi-Pillastrini, G. Chincarini, G. Vettolani, and G. Zamorani, *Nature* **338**, 562 (1989).
- S. Raychaudhury, *Nature* **342**, 251 (1989).
- H. M. Courtois, D. Pomarède, R. B. Tully, Y. Hoffman, and D. Courtois, *AJ* **146**, 69 (2013), arXiv:1306.0091 [astro-ph.CO].
- R. B. Tully, H. Courtois, Y. Hoffman, and D. Pomarède, *Nature* **513**, 71 (2014), arXiv:1409.0880 [astro-ph.CO].
- R. B. Tully, D. Pomarède, R. Graziani, H. M. Courtois, Y. Hoffman, and E. J. Shaya, *ApJ* **880**, 24 (2019), arXiv:1905.08329 [astro-ph.CO].
- H. M. Courtois, A. Dupuy, D. Guinet, G. Baulieu, F. Ruppin, and P. Brenas, *A&A* **670**, L15 (2023), arXiv:2211.16390 [astro-ph.CO].
- R. B. Tully, E. Kourkchi, H. M. Courtois, G. S. Anand, J. P. Blakeslee, D. Brout, T. d. Jaeger, A. Dupuy, D. Guinet, C. Howlett, J. B. Jensen, D. Pomarède, L. Rizzi, D. Rubin, K. Said, D. Scolnic, and B. E. Stahl, *ApJ* **944**, 94 (2023), arXiv:2209.11238 [astro-ph.CO].
- Y. Hoffman, A. Valade, N. I. Libeskind, J. G. Sorce, R. B. Tully, S. Pfeifer, S. Gottlöber, and D. Pomarède, *MNRAS* **527**, 3788 (2024), arXiv:2311.01340 [astro-ph.CO].
- H. M. Courtois, J. Mould, A. M. Hollinger, A. Dupuy, and C. P. Zhang, *A&A* **701**, A187 (2025), arXiv:2502.01308 [astro-ph.CO].
- A. Valade, N. I. Libeskind, D. Pomarède, R. B. Tully, Y. Hoffman, S. Pfeifer, and E. Kourkchi, *Nature Astronomy* **8**, 1610 (2024), arXiv:2409.17261 [astro-ph.CO].
- A. Dupuy, D. Jeong, S. E. Hong, H. S. Hwang, J. Kim, and H. M. Courtois, arXiv e-prints, arXiv:2511.03919 (2025), arXiv:2511.03919 [astro-ph.CO].
- A. Dupuy and H. M. Courtois, *A&A* **678**, A176 (2023), arXiv:2305.02339 [astro-ph.CO].
- Planck Collaboration, N. Aghanim, Y. Akrami, et al., *A&A* **641**, A1 (2020a), arXiv:1807.06205 [astro-ph.CO].
- Y. Hoffman, D. Pomarède, R. B. Tully, and H. M. Courtois, *Nature Astronomy* **1**, 0036 (2017), arXiv:1702.02483 [astro-ph.CO].
- E. J. Shaya, P. J. E. Peebles, and R. B. Tully, *ApJ* **454**, 15 (1995), arXiv:astro-ph/9506144 [astro-ph].
- E. J. Shaya, R. B. Tully, Y. Hoffman, and D. Pomarède, *ApJ* **850**, 207 (2017), arXiv:1710.08935 [astro-ph.CO].
- E. J. Shaya, R. B. Tully, D. Pomarède, and A. Peel, *ApJ* **927**, 168 (2022), arXiv:2201.12315 [astro-ph.CO].
- J. Jasche and B. D. Wandelt, *MNRAS* **432**, 894 (2013), arXiv:1203.3639 [astro-ph.CO].
- S. McAlpine, J. Jasche, M. Ata, G. Lavaux, R. Stiskalek, C. S. Frenk, and A. Jenkins, *MNRAS* **540**, 716 (2025), arXiv:2505.10682 [astro-ph.CO].
- G. Lavaux and M. J. Hudson, *MNRAS* **416**, 2840 (2011), arXiv:1105.6107 [astro-ph.CO].
- R. Stiskalek, H. Desmond, J. Devriendt, A. Slyz, G. Lavaux, M. J. Hudson, D. J. Bartlett, and H. M. Courtois, *MNRAS* (2025), 10.1093/mnras/staf1960, arXiv:2502.00121 [astro-ph.CO].
- A. Dupuy, H. M. Courtois, F. Dupont, F. Denis, R. Graziani, Y. Copin, D. Pomarède, N. Libeskind, E. Carlesi, B. Tully, and D. Guinet, *MNRAS* **489**, L1 (2019), arXiv:1907.06555 [astro-ph.CO].
- A. Dupuy, H. M. Courtois, N. I. Libeskind, and D. Guinet, *MNRAS* **493**, 3513 (2020), arXiv:2002.06814 [astro-ph.CO].
- E. Wempe, G. Lavaux, S. D. M. White, A. Helmi, J. Jasche, and S. Stopyra, *A&A* **691**, A348 (2024), arXiv:2406.02228 [astro-ph.GA].
- E. Wempe, A. Helmi, S. D. M. White, J. Jasche, and G. Lavaux, *A&A* **701**, A178 (2025), arXiv:2501.08089 [astro-ph.GA].
- J. Jasche, F. Leclercq, and B. D. Wandelt, *J. Cosmology Astropart. Phys.* **2015**, 036 (2015), arXiv:1409.6308 [astro-ph.CO].
- G. Lavaux and J. Jasche, *MNRAS* **455**, 3169 (2016), arXiv:1509.05040 [astro-ph.CO].
- F. Leclercq, J. Jasche, G. Lavaux, B. Wandelt, and W. Percival, *J. Cosmology Astropart. Phys.* **2017**, 049 (2017), arXiv:1601.00093 [astro-ph.CO].
- G. Lavaux, J. Jasche, and F. Leclercq, arXiv e-prints, arXiv:1909.06396 (2019), arXiv:1909.06396 [astro-ph.CO].
- N. Porqueres, D. Kodi Ramanah, J. Jasche, and G. Lavaux, *A&A* **624**, A115 (2019), arXiv:1812.05113 [astro-ph.CO].
- S. Stopyra, H. V. Peiris, A. Pontzen, J. Jasche, and G. Lavaux, *MNRAS* **527**, 1244 (2024), arXiv:2304.09193 [astro-ph.CO].
- M. Schaller, J. Borrow, P. W. Draper, M. Ivkovic, S. McAlpine, B. Vandenbroucke, Y. Bahé, E. Chaikin, A. B. G. Chalk, T. K. Chan, C. Correa, M. van Daalen, W. Elbers, P. Gonnet, L. Hausammann, J. Helly, F. Huško, J. A. Kegerreis, F. S. J. Nobels, S. Ploekinger, Y. Revaz, W. J. Roper, S. Ruiz-Bonilla, T. D. Sandnes, Y. Uyttenhove, J. S. Willis, and Z. Xiang, *MNRAS* **530**, 2378 (2024), arXiv:2305.13380 [astro-ph.IM].
- T. M. C. Abbott, M. Aguena, A. Alarcon, S. Allam, O. Alves, A. Amon, F. Andrade-Oliveira, J. Annis, S. Avila, D. Bacon, et al., *Phys. Rev. D* **105**, 023520 (2022), arXiv:2105.13549 [astro-ph.CO].
- S. McAlpine, arXiv e-prints, arXiv:2510.16574 (2025), arXiv:2510.16574 [astro-ph.CO].
- J. J. Monaghan, *ARA&A* **30**, 543 (1992).
- S. Colombi, M. J. Chodorowski, and R. Teyssier, *MNRAS* **375**, 348 (2007), arXiv:0805.1693 [astro-ph].
- F. Villaescusa-Navarro, C. Hahn, E. Massara, A. Banerjee, A. M. Delgado, D. K. Ramanah, T. Charnock, E. Giusarma, Y. Li, E. Allys, A. Brochard, C. Uhlemann, C.-T. Chiang, S. He, A. Pisani, A. Obuljen, Y. Feng, E. Castorina, G. Contardo, C. D. Kreisch, A. Nicola, J. Alsing, R. Scoccimarro, L. Verde, M. Viel, S. Ho, S. Mallat, B. Wandelt, and D. N. Spergel, *ApJS* **250**, 2 (2020), arXiv:1909.05273 [astro-ph.CO].
- V. Springel, *MNRAS* **364**, 1105 (2005), arXiv:astro-ph/0505010 [astro-ph].
- Planck Collaboration, N. Aghanim, Y. Akrami, M. Ashdown, J. Aumont, C. Baccigalupi, M. Ballardini, A. J. Banday, R. B. Barreiro, N. Bartolo, et al., *A&A* **641**, A6 (2020b), arXiv:1807.06209 [astro-ph.CO].
- P. J. E. Peebles, *The large-scale structure of the universe* (1980).
- F. R. Bouchet, S. Colombi, E. Hivon, and R. Juszkiewicz, *A&A* **296**, 575 (1995), arXiv:astro-ph/9406013 [astro-ph].
- L. Wang and P. J. Steinhardt, *ApJ* **508**, 483 (1998), arXiv:astro-ph/9804015 [astro-ph].
- V. Springel, R. Pakmor, O. Zier, and M. Reinecke, *MNRAS* **506**, 2871 (2021), arXiv:2010.03567 [astro-ph.IM].
- M. Davis, G. Efstathiou, C. S. Frenk, and S. D. M. White, *ApJ* **292**, 371 (1985).
- P. A. Woudt and R. C. Kraan-Korteweg, in *Mapping the Hidden Universe: The Universe behind the Milky Way - The Universe in HI*, Astronomical Society of the Pacific Conference Series, Vol. 218, edited by R. C. Kraan-Korteweg, P. A. Henning, and H. Andernach (2000) p. 193, arXiv:astro-ph/0006126 [astro-ph].
- E. Kourkchi, R. B. Tully, G. S. Anand, H. M. Courtois, A. Dupuy, J. D. Neill, L. Rizzi, and M. Seibert, *ApJ* **896**, 3 (2020), arXiv:2004.14499 [astro-ph.GA].
- A. M. Hollinger and M. J. Hudson, *MNRAS* **531**, 788 (2024), arXiv:2312.03904 [astro-ph.CO].
- Planck Collaboration, *A&A* **641**, A1 (2020), arXiv:1807.06205 [astro-ph.CO].
- N. Trentham, R. B. Tully, and M. A. W. Verheijen, *MNRAS* **325**, 385 (2001), arXiv:astro-ph/0103039 [astro-ph].
- G. Lavaux, R. B. Tully, R. Mohayaee, and S. Colombi, *ApJ* **709**, 483 (2010), arXiv:0810.3658 [astro-ph].
- R. B. Tully, E. J. Shaya, I. D. Karachentsev, H. M. Courtois, D. D. Kocevski, L. Rizzi, and A. Peel, *ApJ* **676**, 184 (2008), arXiv:0705.4139.
- J. A. Peacock, *MNRAS* **258**, 581 (1992).
- D. Benisty, E. Vasiliev, N. W. Evans, A.-C. Davis, O. V. Hartl, and L. E. Strigari, *ApJ* **928**, L5 (2022), arXiv:2202.00033 [astro-ph.GA].

plement the main text. Firstly, in Fig. 9 we show the standard deviation of the cGA basin depth across the 80

APPENDIX

A. FURTHER VISUALISATION OF THE CGA REGION

Here we briefly present additional figures visualising the cGA region identified in *Manticore-Local*, to sup-

Manticore-Local realisations, complementing the mean depth shown in Fig. 3. Secondly, Fig. 10 presents the sky-projected mean density field, obtained by averaging the 80 **Manticore-Local** realisations and, for each pixel, computing

$$\langle \rho \rangle_{\text{sky}} = \frac{\int_0^{80 h^{-1} \text{Mpc}} r^2 \rho(r, \ell, b) dr}{\int_0^{80 h^{-1} \text{Mpc}} r^2 dr}, \quad (\text{A1})$$

which integrates $r^2 \rho$ along the line of sight to $80 h^{-1} \text{Mpc}$ (approximately the maximal cGA extent from the observer) and normalises by the corresponding volume factor.

This paper was built using the Open Journal of Astrophysics L^AT_EX template. The OJA is a journal which provides fast and easy peer review for new papers in the **astro-ph** section of the arXiv, making the reviewing process simpler for authors and referees alike. Learn more at <http://astro.theoj.org>.

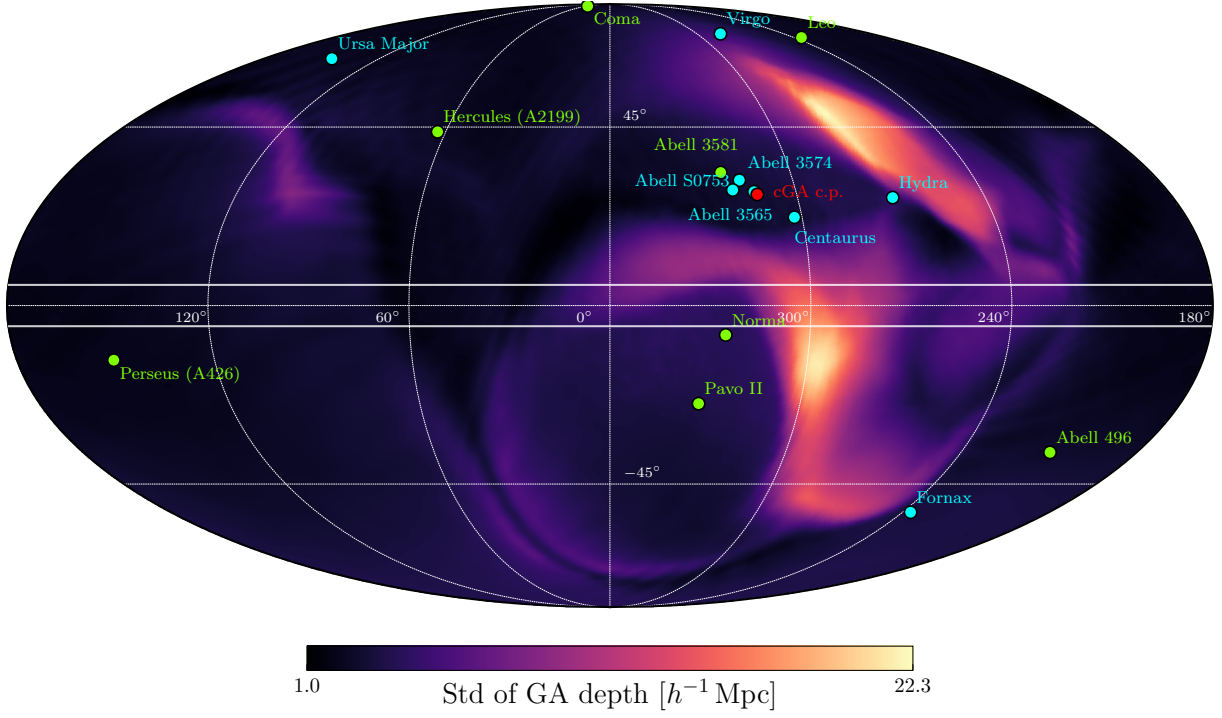


Figure 9 Standard deviation of the cGA basin depth across 80 Manticore-Local realisations at $\sigma_{\text{smooth}} = 3 h^{-1} \text{ Mpc}$, complementing the mean depth shown in Fig. 3. Variance is smallest toward the cGA direction and largest along the basin boundary, highlighting where the attractor’s extent is most and least certain; the ZoA (white lines at $b = \pm 5$ deg) is retained for reference. Dashed white lines indicate meridians every 60 deg and parallels at ± 45 deg.

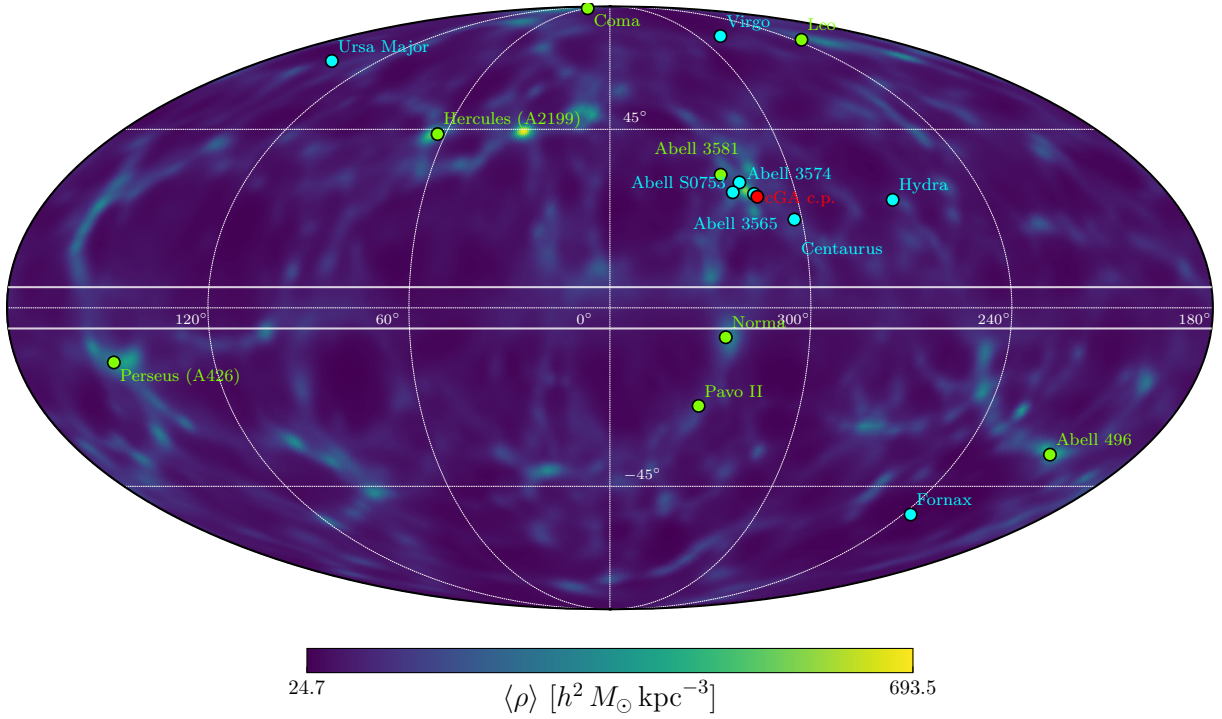


Figure 10 Sky-projected mean density field at $\sigma_{\text{smooth}} = 3 h^{-1} \text{ Mpc}$, computed by averaging the 80 Manticore-Local realisations and, for each sky pixel, evaluating $\langle \rho \rangle_{\text{sky}} = [\int_0^{80 h^{-1} \text{ Mpc}} r^2 \rho(r, \ell, b) dr] / [\int_0^{80 h^{-1} \text{ Mpc}} r^2 dr]$. The map highlights the projected overdensities associated with the cGA region and surrounding structures in Galactic coordinates; density within the ZoA (white lines at $b = \pm 5$ deg) appears blurrier, though coherent structure persists across it. Dashed white lines indicate meridians every 60 deg and parallels at ± 45 deg.